Volatile and Sr Isotope Analysis of Melt Inclusions from the Bandelier Tuff, Valles Caldera, New Mexico: Insights into Pre-Eruptive Magma Conditions

by

Jennifer H. Cartwright

A thesis submitted to the Graduate Faculty of
Auburn University
in partial fulfillment of the
requirements for the Degree of
Master of Science

Auburn, Alabama
May 5, 2018

Approved by

Haibo Zou, Chair, Professor of Geosciences
Mark G. Steltenpohl, Professor of Geosciences
Willis E. Hames, Professor of Geosciences

ABSTRACT

The Valles Caldera, located in northwest New Mexico, is one of three caldera volcanoes in the United States that is still active today. Calderas have the largest, most cataclysmic eruptions that result in large bowl-shaped depressions. Calderas are still not completely understood so studying their byproducts can not only give insights into pre-eruptive magma conditions of past eruptions but also provide insights into the behavior of future eruptions. An extremely useful tool to utilize for such studies is melt inclusions. Melt inclusions are small amounts of melt that were trapped at magmatic temperatures and pressures and potentially preserve pre-eruptive conditions.

In order to gain more insights into the pre-eruptive magma conditions of the Valles Caldera, this study analyzed melt inclusions from the Lower and Upper Bandelier Tuff, which resulted from the two caldera forming events at 1.6 Ma and 1.2 Ma. Volatile contents (S and H_2O), major elements and $^{87}Sr/^{86}Sr$ ratios of melt inclusions were measured. $^{87}Sr/^{86}Sr$ ratios revealed that melt inclusions represent bulk magma compositions and suggest a mantle-derived magma recharge event between the Lower and Upper Bandelier Tuff eruptions. Electron microprobe analysis results show high H_2O content and low S content for the melt inclusions in pumices from the base of the Lower Bandelier and the base of the Upper Bandelier. These volatile contents indicate that both Bandelier eruptions were very explosive as a result of high H_2O contents, but did not have much effect on global cooling as suggested by their low S contents. As for future eruptions, if these volatile trends (high H_2O and low S) continue, then the behavior of such eruptions would behave in a similar fashion.

ACKOWLEDGMENTS

I would like to express my sincere gratitude to my advisor Dr. Haibo Zou for his constant mentorship throughout my time at Auburn. Dr. Zou was always available when I had questions or needed help, and he always made it a point to assure me that my thesis was one of his priorities. This was most apparent when he accompanied me on an 8-day trip during his very short break between summer and fall semester where he drove us to and from New Mexico so that I could collect samples for this study. It is an act of kindness and an adventure I will never forget. Without Dr. Zou's patience, valuable knowledge, funding, and encouragement, this accomplishment would have been very hard to achieve.

I am thankful to Dr. Robert Parmenter from National Park Service for his approval of a research permit for the Valles Caldera National Reserve. I also owe many thanks to my committee members, Dr. Bill Hames and Dr. Mark Steltenpohl. The electron microprobe work and grain mount polishing would not have been possible without the guidance of Dr. Hames. And thank you to Dr. Steltenpohl for his enthusiasm and review of my research.

This study was funded in part by the Department of Geosciences through the Spencer Waters and Dan Folse Memorial Award, by the Auburn University Geosciences Advisory Board through a student research grant, and by the Intramural Grants Program (#16-125) of the Office of the Vice President for Research and Economic Development.

Finally, I would like to thank my family and friends. To my parents Ann and Lon, thank you for always supporting me, guiding me and for all that you have done for me in life. To my friends back at home, thank you for always making me laugh and letting me know that you can’twait for me to come back to Texas. And to my new friends here in Auburn, thank you for being an incredible part of my graduate school experience.

TABLE OF CONTENTS

LIST OF TABLES

LIST OF FIGURES

INTRODUCTION

Volcanic eruptions can have many effects on the area surrounding a volcano. One type of volcano that has particularly dangerous eruptions is a caldera volcano. Calderas have the largest, most explosive eruptions and are associated with voluminous ash-flows (Lipman 1977). These violent eruptions result in large bowl-shaped depressions that can be several miles in diameter (Chipera et al. 2008). Caldera eruptions have caused drastic effects on nature in the past and are still not completely understood. For these reasons, scientists are studying evidence from past eruptions in order to infer the behavior of future eruptions.

One way to analyze evidence from past eruptions is through melt inclusions. Melt inclusions are found in phenocrysts of volcanic rocks. They are small amounts of melt (typically 1 – 100 microns in diameter) that were trapped at magmatic temperatures and pressures (Bacon et al. 1992; Stefano et al. 2011; Cannatelli et al. 2016). Once melt inclusions form in a host mineral, they become isolated from the magmatic environment and act as a closed system. Therefore, these inclusions potentially preserve the compositions of magma during a specific stage of its evolution that the host mineral grew in and provide a direct way to measure pre-eruptive conditions and contents of the magma (Bacon et al. 1992; Wallace et al. 1999; Frezzotti 2001; Stefano et al. 2011). Volatiles (S, Cl, F, and water) in melt inclusions provide information on pre-eruptive magma conditions as well as how these conditions change over time (Bacon et al. 1992; Dunbar and Hervig 1992). Volatile contents can also give insights into the effect a past eruption had on nature and the effect a future eruption could have on nature, including people (Bacon et al. 1992; Stimac et al. 1996).

It is important to couple volatile analysis with Sr isotope analysis of melt inclusions when studying erupted magmas preserved in pumice. Analyzing Sr isotopic compositions of melt inclusions and bulk pumice is useful in evaluating the relationship between the magma in melt inclusions and the erupted magma.

A well-known example of a resurgent caldera in the United States is the Valles Caldera in northwestern New Mexico (Fig. 1). Hydrothermal activity around the Valles Caldera suggests that it is still active today (Goff and Gardner 2004). Since the Valles Caldera is still active and could potentially have a future eruption, it is important to understand how the next eruption might behave and the effects it could have on the surrounding area by studying the behavior of past eruptions. In order to do so, this study analyzed the Lower and Upper Bandelier Tuff units, which resulted from the two caldera-forming explosions. Major elements and sulfur concentrations of melt inclusions as well as $^{87}Sr/^{86}Sr$ content of melt inclusions and whole rock pumice from the Bandelier Tuff are reported.

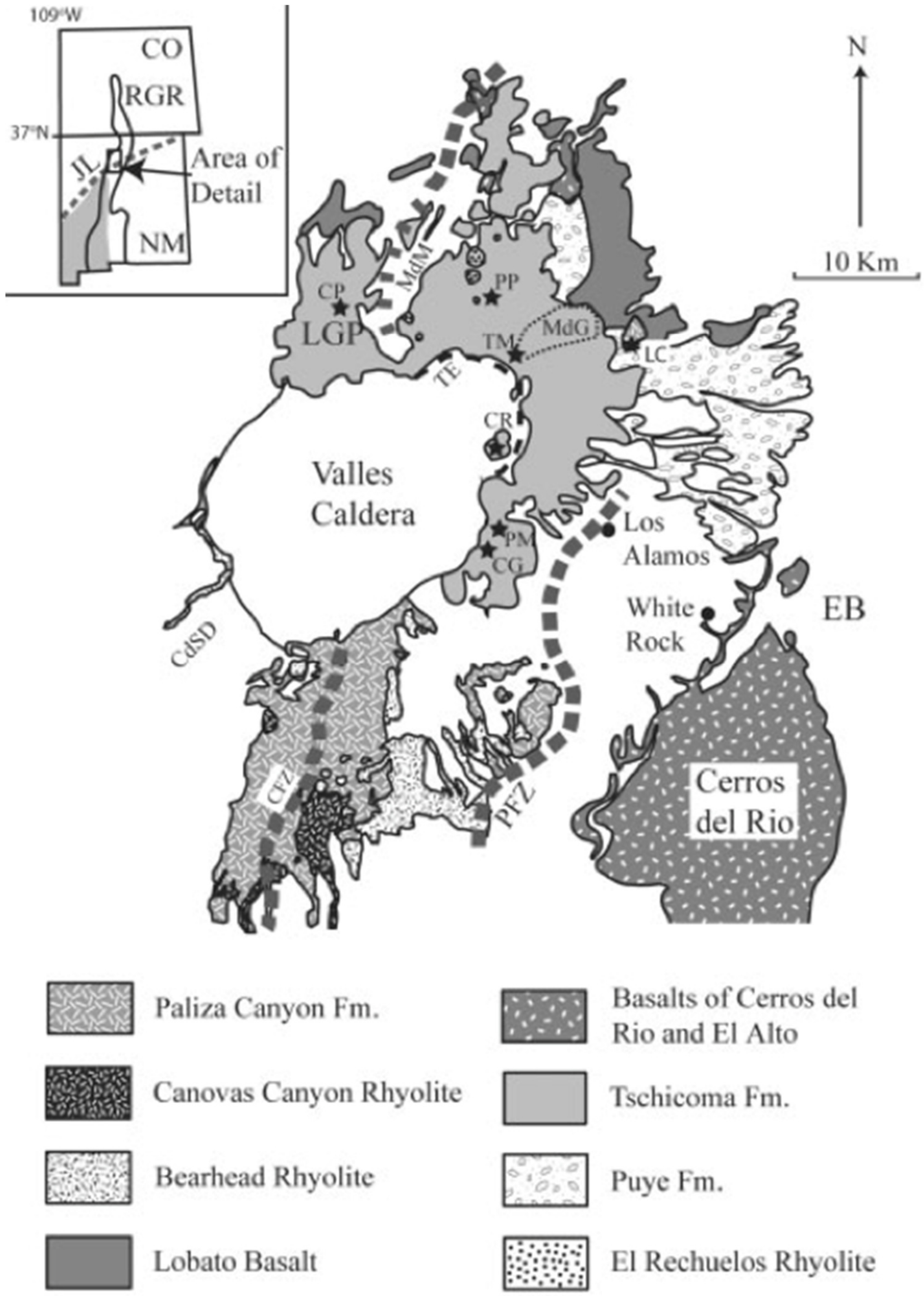

Fig. 1. Generalized map showing the location of the Valles Caldera and surrounding geology. CP = Cerro Pavo; MdM = Mesa del Medio; PP = Polvadera Peak; TM = Tschicoma Mountain; MdG = Mesa de la Gallina; LC = Los Cerro; TE = Toldeo Embayment; CR = Cerro Runio; PM = Parajito Mt.; CG = Cerro Grande; LGP = La Grulla Plateau; CdSD = Canon de San Diego; EB = Espanola basin; PFZ = Parajito fault zone; CFZ = Canada de Cochiti fault zone; RGR = Rio Grande rift; JL = Jemez lineament (Rowe et al. 2007).

OBJECTIVES

This research focuses on pre-eruptive magmatic conditions of the caldera-forming event of the Valles Caldera. These pre-eruptive conditions can be acquired through analysis of melt inclusions from the Bandelier Tuff. Few studies have been conducted on the volatile content of melt inclusions from the Upper Bandelier tuff and no study has paired volatile and Sr isotope analysis of both members of the Bandelier Tuff. By conducting this analysis, better constraints can be given to the pre-eruptive magmatic conditions and help predict the behavior of potential future eruptions.

These objectives were achieved by (1) measuring $^{87}Sr/^{86}Sr$ of melt inclusions and whole rock pumice to determine that the melt inclusion non-volatile compositions are similar to the bulk magma compositions, and (2) using the electron microprobe to measure pre-eruption volatile (S and H_2O) and major element compositions.

BACKGROUND

Geologic Setting

The area containing the Valles Caldera was purchased by the U.S. Government and made into a national preserve in 2000 (Chipera et al. 2008). The purpose of the Valles Caldera National Preserve is to protect the caldera's geology and to promote scientific investigations of the area (Chipera et al. 2008). The Valles Caldera is part of the Jemez Mountains volcanic field, which is located northwest of Santa Fe and lies within the intersection of the Jemez Lineament and the Rio Grande rift (Fig. 2) (Golombek et al. 1983; Dunbar and Hervig 1992). The Jemez Lineament is a crustal flaw that traces northeast to southwest and volcanically active from the Miocene to the present (Phillips et al. 2007). The north-south-trending Rio Grande rift began to form due to crustal extension beginning in the Oligocene and is still on going today (Golombek et al. 1983). This crustal extension caused multiple episodes of volcanism in the Jemez Mountains with basaltic, andesitic, dacitic and rhyolitic compositions (Goff and Janik 2002; Wilcock et al. 2013). This volcanism peaked with the episodes that created the Toledo/Valles Caldera complex, which produced the Bandelier Tuff (Fig. 3). The Bandelier Tuff is divided into upper and lower members that are associated with the two separate caldera-forming events. The Toledo Caldera (Fig. 4) formed first from a violent explosion of rhyolitic magma at ~ 1.6 Ma (Eichelberger and Koch 1979). This eruption produced the Otowi Member or Lower Bandelier Tuff (LBT) and it is estimated that a volume of 400 km^3 of dense rock equivalent (DRE) of the tuff was erupted (Wolff et al. 2002). At ~ 1.2 Ma another rhyolitic magmatic event occurred and created the 22-km diameter Valles Caldera, which overprints most of the Toledo Caldera (Fig. 4)

(Eichelberger and Koch 1979; Wolff et al. 2002). This event produced the Tshirege Member or Upper Bandelier Tuff (UBT), which disconformably overlies the Otowi Member and had an eruptive volume of 400 km^3 DRE (Crowe et al. 1978; Goff et al. 2014).

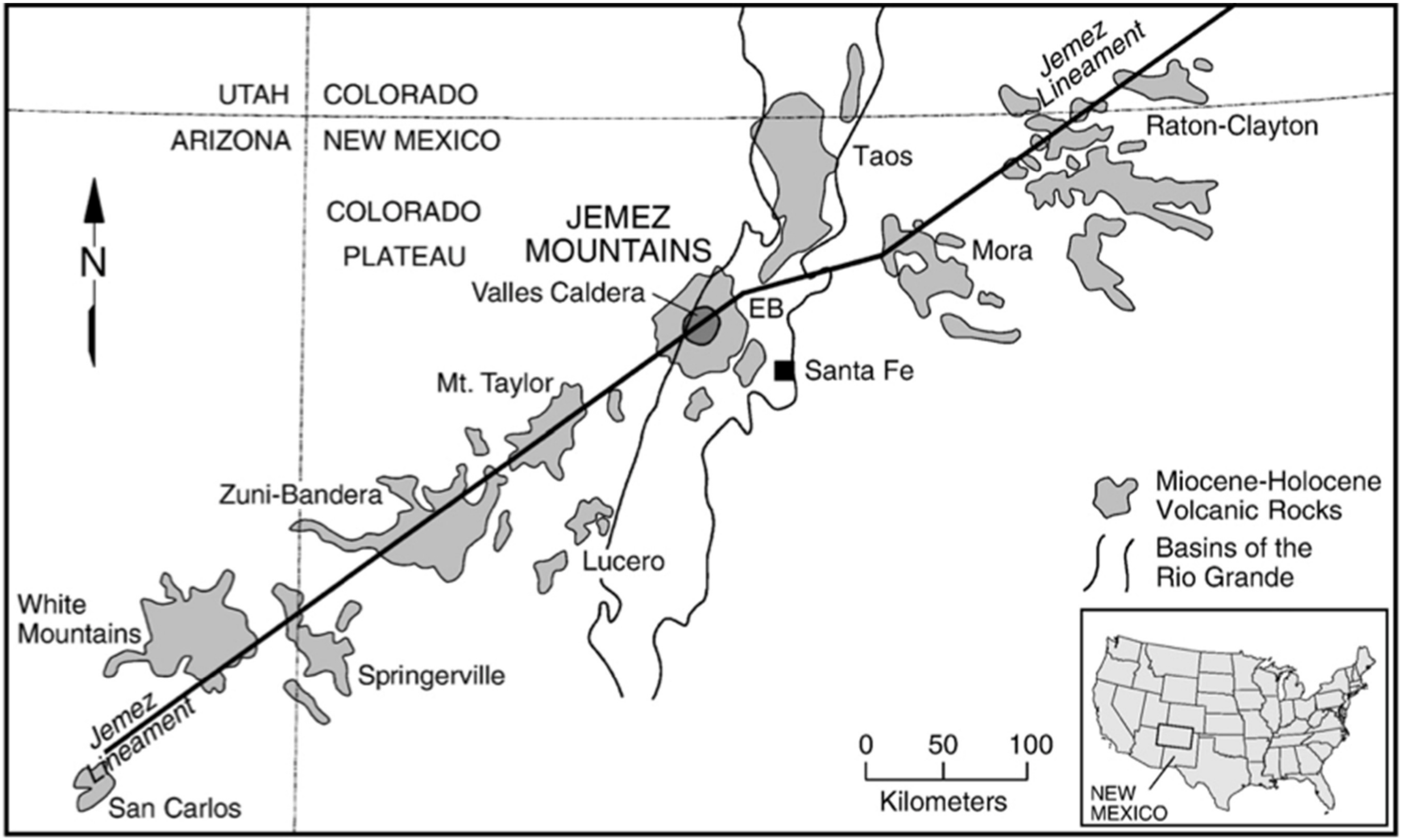

Fig. 2. Regional map showing Jemez Mountains and Valles Caldera with respect to the Jemez Lineament and Rio Grande rift. EB = Espanola Basin (Goff and Gardner 2004).

Fig. 3. Map of the Valles Caldera and distribution of the Bandelier Tuff. Stars represent locations where samples were collected for this study.

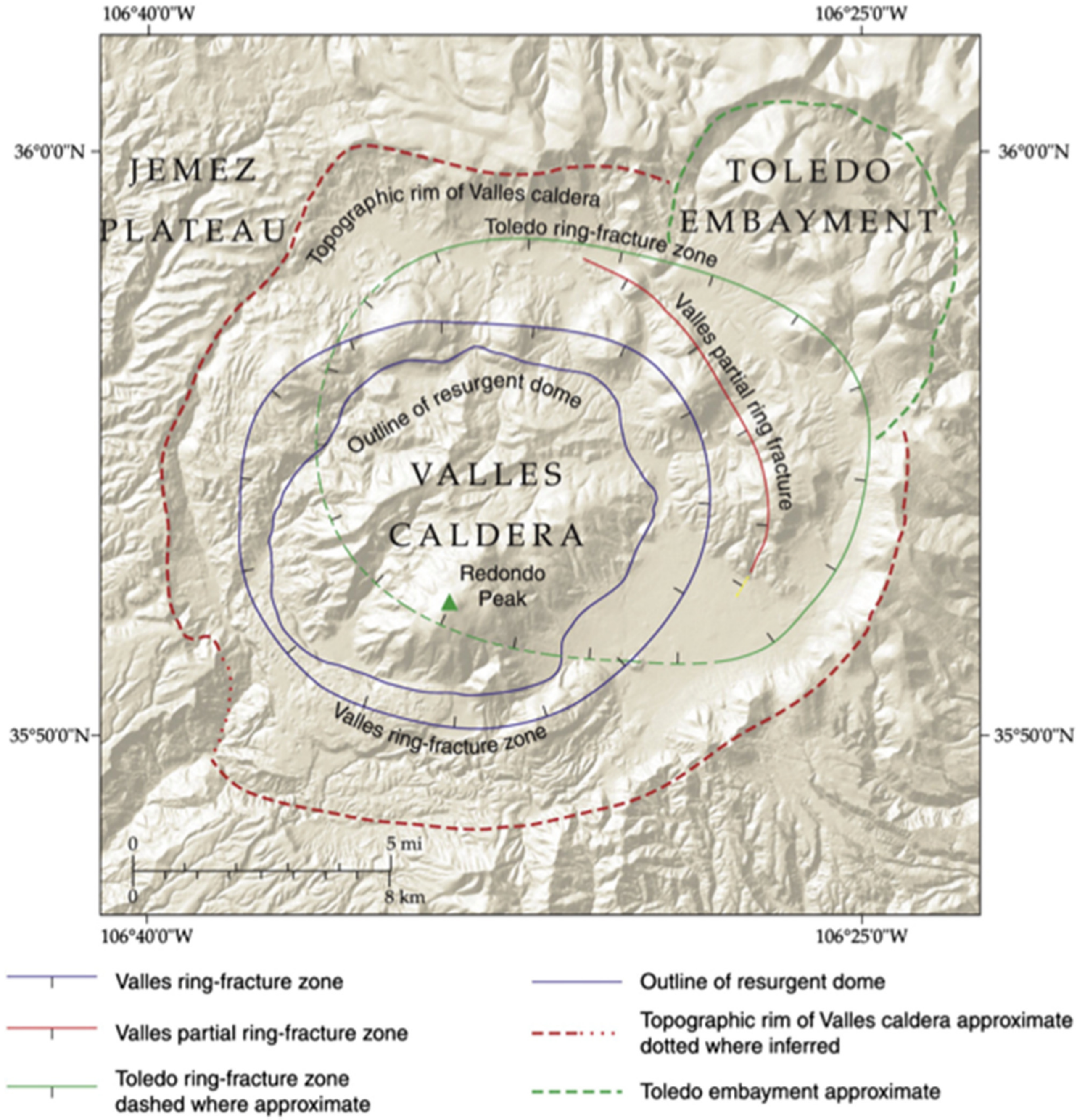

Fig. 4. Map depicting the remnants of both the Toledo and Valles Caldera eruptions (Goff et al. 2014).

The Otowi Member (LBT) consists of a basal pyroclastic fall deposit called the Guaje Pumice and is overlain by intracaldera ignimbrites (ash flows) (Goff and Gardner 2004; Cook et al. 2016). These units have compositions that show they were produced from a zoned magma system of high silica rhyolite (>75 wt% SiO_2) (Self at al. 1996; Cook et al. 2016). There are stratigraphic variations in minor and incompatible trace elements in the units first erupted to the units last erupted (Self at al. 1996; Cook et al. 2016). The welding of the units in the Otowi Member range from poorly welded to non-welded (Stimac et al. 1996). The assemblage of phenocrysts consists of mostly quartz and sanidine (95%) with minor amounts of hedenbergite, magnetite, zircon, allanite, fayalite and chevkinite (Wolff and Ramos 2014).

The Tshirege Member (UBT) consists of a basal pyroclastic fall deposit called the Tsankawi Pumice that is overlain by ignimbrite flow units (Goff and Gardner 2004; Cook et al. 2016). This member was also produced from a compositionally zoned high silica rhyolite (Cook et al. 2016). At the base, the Tshirege Member has a high silica rhyolite composition and moving upward stratigraphically its composition becomes more of a low-silica rhyolite (72 wt% SiO_2) (Stimac et al. 1996). The Tshirege Member has units that range from non-welded to densely welded (Stimac et al. 1996). Phenocrysts in the unit include sanidine, quartz, and anorthoclase, with low amounts of plagioclase, mafic minerals, apatite, zircon and chevkinite (Goff et al. 2014).

Melt Inclusions

In the past, studies on melt inclusions were not common because there were not many reliable techniques to analyze their contents (Cannatelli et al. 2016). Observations of melt inclusions were first published by Sorby (1858) who gave detailed descriptions and drawings of melt inclusions (Fig. 5). Sorby (1858) theorized that melt inclusions could be a potential tool for interpreting the origin of igneous rocks. However, due to the lack of micro-analytical techniques, among other reasons, it wasn't until decades later that scientists would further study melt inclusions. Barrabé and Deicha (1956) ignited interest again by being the first to homogenize melt inclusions in quartz through heating at high temperatures. Improvements in homogenizing and quenching of melt inclusions rapidly followed and scientists began to use melt inclusions for geochemistry and petrology studies of igneous rocks in the 1970s (Hauri et al. 2002; Cannatelli et al. 2016).

With the development and improvement of micro-analytical techniques that allowed trace elements and isotopic composition of samples to be determined, studies on melt inclusions became more common and reliable (Cannatelli et al. 2016). Instruments such as Secondary Ion Mass spectroscopy (SIMS) and Fourier Transform InfraRed spectroscopy (FTIR) allowed scientist to directly measure melt inclusions. In the 1990s melt inclusions became fully accepted as useful tools and melt inclusion studies increased dramactically. Many scientists began to utilize the contents of melt inclusions such as trace elements, isotopes and volatiles to help constrain magmatic processes, origins and eruptive styles (Cannatelli et al. 2016). Melt inclusions add a new element to the big picture of igneous processes because, unlike whole rock, they provide information (composition, temperature, etc.) on a specific time of a melt during the line of liquid descent (Roedder 1979; Frezzotti 2001; Cannatelli et al. 2016).

Even with reliable techniques, such as electron microprobe, LA-ICPMS, Fourier Transform InfraRed spectroscopy and SIMS, analyzing melt inclusions needs to be treated with caution. Melt inclusions do not always represent pre-eruptive conditions or can be compromised by post-entrapment processes (Cannatelli et al. 2016). The most common post-

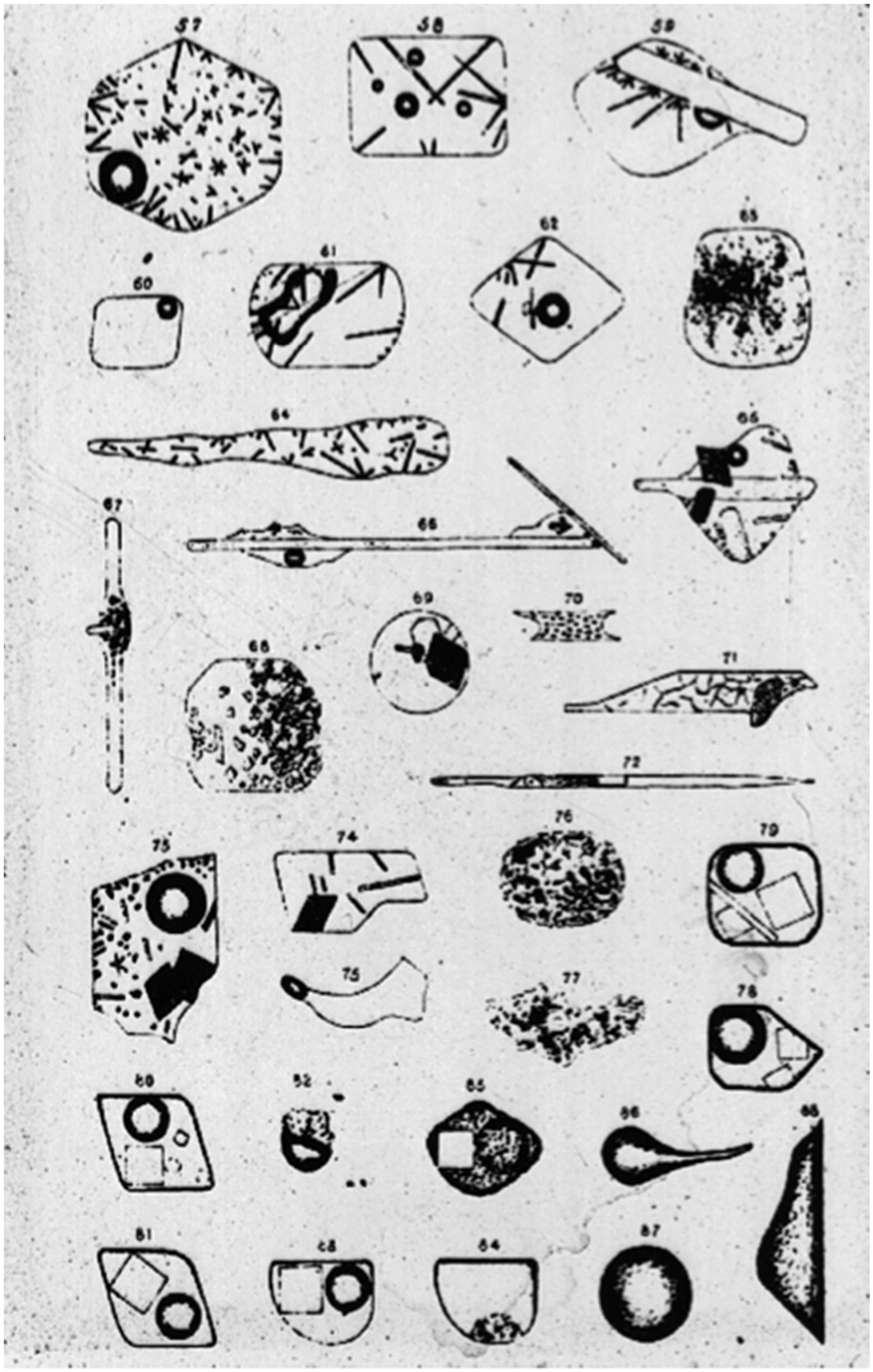

Fig. 5. Original drawings of melt inclusions by Sorby (1858). All melt inclusions drawn have post-entrapment features like bubbles and daughter minerals.

entrapment changes that can affect analysis of melt inclusions are bubbles, crystallization of daughter mineralsf and leakage (Roedder 1979). As an inclusion cools, the melt contracts and depressurizes, which causes volatiles to exsolve and form a “shrinkage” bubble (Roedder 1979). If the melt inclusion is cooled rapidly then it will stay as a single glassy phase and “shrinkage’ bubbles will not occur (Fig. 6) (Roedder 1979). Crystallization of daughter minerals in a melt inclusion occurs during slow cooling and the slower the cooling rate, the more daughter minerals form (Roedder 1979; Student and Bodnar 2004). Completely crystallized melt inclusions are usually dark to opaque and can be accompanied by a bubble (Student and Bodnar 2004). In order to accurately study melt inclusions that are crystallized to any degree, re-homogenization is necessary (Student and Bodnar 2004). Leakage of a melt inclusion occurs when a melt inclusion is no longer a closed system and material can move in or out of the inclusion (Roedder 1979). Leakage due to decrepitation or cracking of a melt inclusion happens when there is a large difference between the external pressure of the host crystal and the internal pressure of the melt inclusion (Roedder 1979). This change in pressure usually occurs during the volcanic eruption but can also happen during heating experiments (Roedder 1979). Leakage can also occur if a melt inclusion is an “hourglass” inclusion (Fig. 7c). “Hourglass” melt inclusions are inclusions that are connected to the outside of the host mineral by a narrow canal.

To avoid these potential obstacles, a detailed assessment of melt inclusions needs to be done in order to find quality samples that will have useful and informative data. Roedder (1984) states that any viable melt inclusion must follow Roedder’s rules: 1) must be trapped as a single homogenous phase; 2) behaved as a closed isochoric system; and 3) after trapping nothing has been added to or lost. Examining melt inclusions through microscopic observation is a necessary step in selecting valid melt inclusions for a study. Noting the size, shape, presence of bubbles

(Fig. 7b) and devitrification minerals (Fig. 7d) in a melt inclusion will help scientists choose melt inclusions that fit best for the study they are conducting and the steps needed to prepare the melt inclusions for analysis (Frezzotti 2001; Cannatelli et al. 2016). If re-heating for homogenization is not available, then it is best to select homogenous glassy melt inclusions (Fig. 7a).

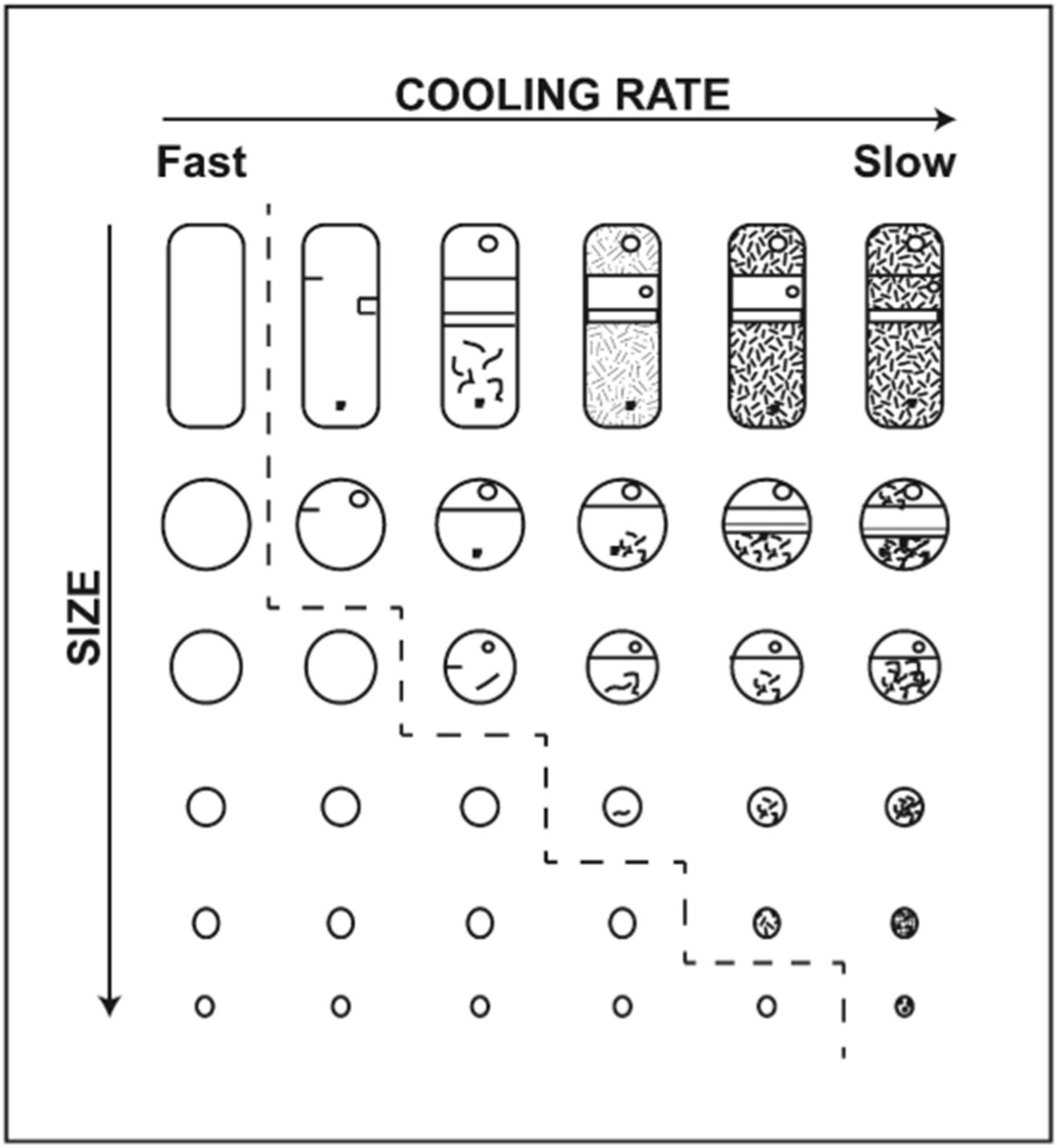

Fig. 6. Schematic diagram showing how cooling rate and size of melt inclusion affect the formation of bubbles and minerals within an inclusion (Modified from Roedder 1984).

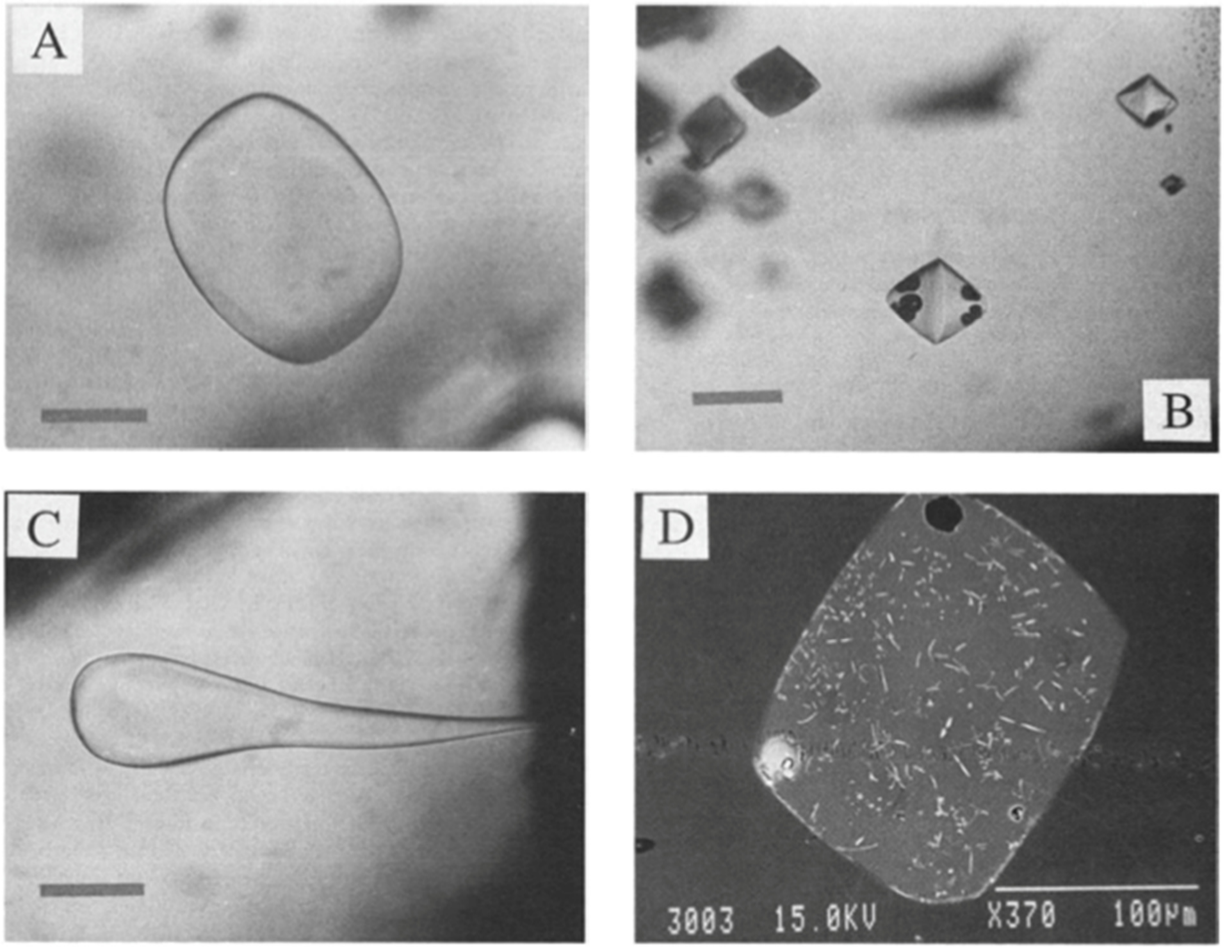

Fig. 7. Examples of melt inclusions in quartz from the Otowi Member of the Bandelier Tuff. A) Homogenous glassy melt inclusion. B) Melt inclusion with bubbles. C) "Hourglass" melt inclusion. D) Back-scattered electron image of a devitrified melt inclusion (Modified from Dunbar and Hervig 1992).

Thermal Ionization Mass Spectrometry

Analysis of radiogenic isotopes is very a useful tool in science and has been used for decades. In geology, radiogenic isotopes have been used in many geochronology and tracer studies. These studies gain valuable information from the isotopic ratios of the U – Pb, Rb – Sr, Nd – Sm and Lu – Hf systems (Potts 1987). In order to use these radiogenic isotopes, they first must be separated from other isotopes, which can be done by a mass spectrometer (Dickin 2005). J.J. Thompson was the first to propose separating positive ions by their mass and the first mass spectrometer to do this was called a "magnetic sector" (Dickin 2005). One mass spectrometer method used for determining precise isotope ratios is thermal ionization mass spectrometry or TIMS. TIMS uses mass spectrometers with thermal ion sources to heat samples and cause ionization of the atoms (Potts 1987). This is done by residues of samples being placed on filaments that are then heated in a vacuum by passing an electric current through it to cause ionization of the atoms in the sample (Potts 1987; Dickin 2005; Faure and Mensing 2005). The resulting positive ions are accelerated across an electric field and focused into beams based on their mass (Fig. 8). The separate isotope beams are collected in Faraday cups where they are converted into voltage. To get the precise isotope ratios, voltages of the collector cups are compared to one another (Dickin 2005).

Certain precautions, like extensive chemical purification, must be taken so that TIMS analysis does not produce inaccurate data. When conducting Sr isotope analysis, it is important to remove major elements and Rb because they can cause drastic isobaric interference problems with the Sr data (Dickin 2005). Chemical purification and extraction of the sample from the matrix of a rock is the only way TIMS analysis is effective (Dickin 2005). This is can be done by first dissolving samples in hot (100 °C) concentrated hydrofluoric acid and nitric acid, which prepares the sample for ion exchange separation (Dickin 2005). Traditionally, the ion separation is done on a cation exchange column partly filled with cation resin. The sample solution is placed into the column, washed through with solvent until the desired element is released (Dickin 2005). In general, elements are removed in the following order: Fe, Na, Mg, K, Rb, Ca, Sr, and Ba. A novel development of Sr-selective resin by Eichrom Technologies allows the use of simpler extraction chromatography to separate Sr from the sample solution (Horwitz et al. 1992).

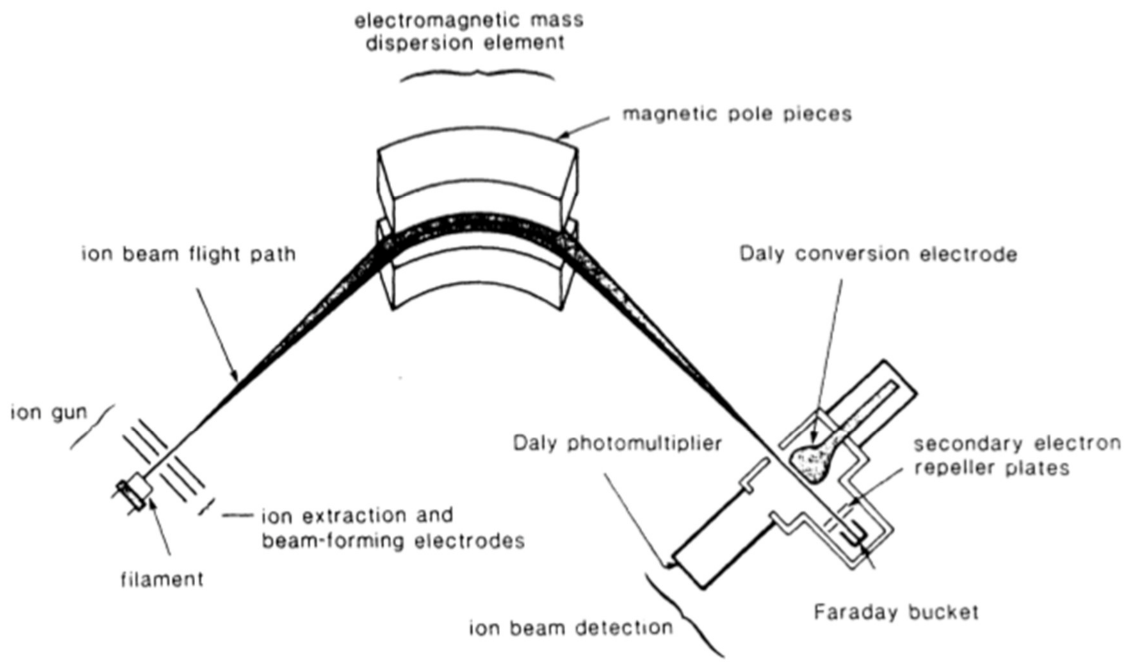

Fig. 8. Schematic diagram of a thermal ionization mass spectrometer (Potts 1987).

Sr Isotope Analysis

For this study TIMS will be utilized for Sr isotope analysis. Isotope studies are fundamental in the origin and formation of igneous rocks. Radiogenic isotopes are caused by the radioactive decay of elements and frequently survive chemical fractionation during a magma's evolution (Wilson 1989). This means that a magma will have the distinct isotopic composition of its source even as it goes through the process of fractional crystallization (Wilson 1989). A magma's isotopic composition will stay constant unless there is contamination through injection or assimilation of an isotopically different magma (Wilson 1989). However, the continental crust and the mantle have very different isotopic (radiogenic and stable) compositions which helps constrain the amount of contamination a magma might have received (Wilson 1989). In fact, these distinct isotopic compositions are the basis when conducting tracer studies, especially when using the Rb – Sr radiogenic system.

Through beta emission ^{87}Rb decays to stable ^{87}Sr and Sr has four naturally occurring isotopes: ^{88}Sr, ^{87}Sr, ^{86}Sr, and ^{84}Sr. Tracer studies use the $^{87}Sr/^{86}Sr$ ratio due to its different signatures in the mantle and crust. Crustal rocks typically have a Rb enrichment compared to Sr, which gives a higher Rb/Sr ratio (Wilson 1989). On the contrary, mantle material is less evolved and has lower Rb/Sr ratios (Wilson 1989). As a result of higher Rb/Sr ratios, accumulation of ^{87}Sr will be greater in the crust than the mantle over time (Fig. 9) (Wilson 1989). Therefore, crustal material develops higher $^{87}Sr/^{86}Sr$ ratios than mantle material. These different $^{87}Sr/^{86}Sr$ ratios allow scientist to trace the effects of contamination of a magma and potentially determine the origin of a material (crustal or mantle derived) (Wilson 1989).

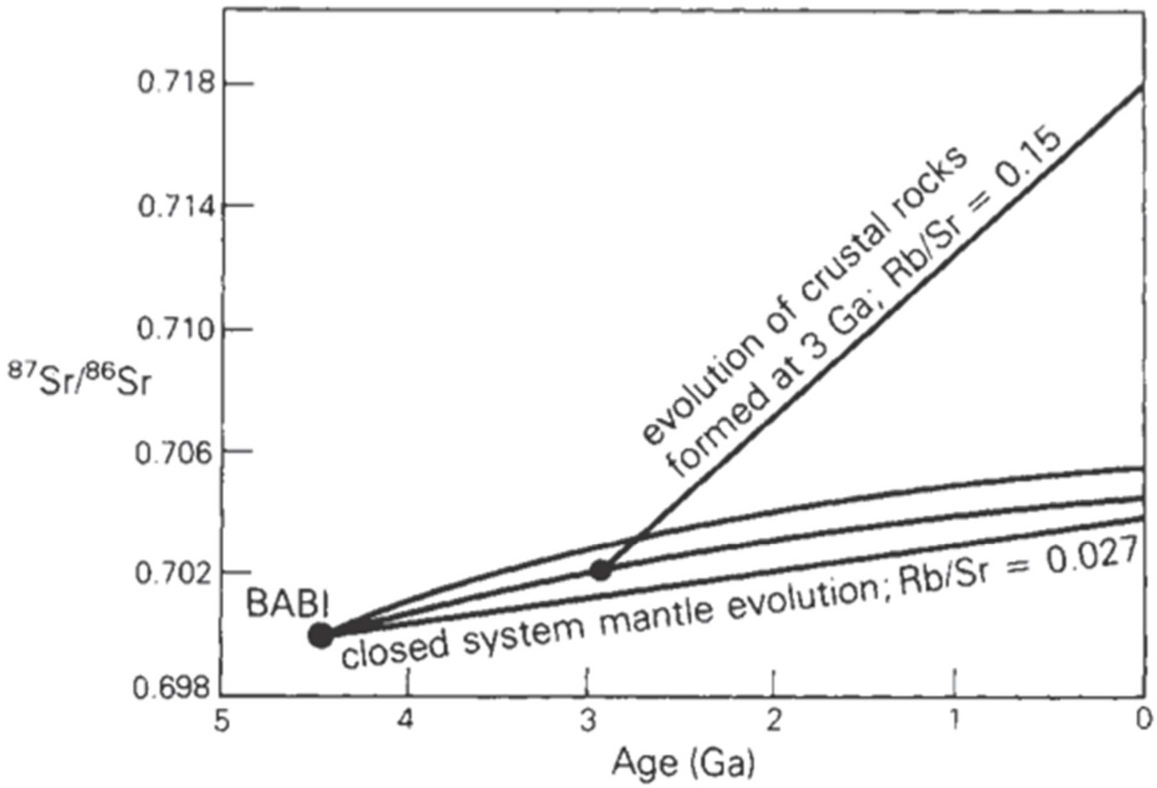

Fig. 9. Illustration showing the evolution of Sr ratios that developed from the primordial value (BABI) (Wilson 1989).

Electron Microprobe

Electron probe microanalysis (EMPA) or electron microprobe analysis is a technique used to determine chemical compositions of minute areas of solid samples. An electron microprobe is essentially the same as a scanning electron microscope (used for imaging) but with the addition of wavelength dispersive spectrometers (WDS) that enable quantitative chemical analysis (Fig. 10). To conduct analysis, an electron microprobe uses a focused electron beam on the surface of a sample (Reed 2005). The beam produces several interactions, some of which cause emission of characteristic X-rays, with the atoms in the sample, that can then be detected and provide information on sample composition (Fig. 11) (Reed 2005). Elements in a sample are identified by their X-ray spectrum that contains specific emissions for each element (Reed 2005). Chemical compositions are determined by comparing intensities of the X-ray emission lines from a sample to the intensities of X-ray emission lines of a standard whose composition is known (Reed 2005). An electron microprobe can quantitatively measure all elements except for H, He, and Li and produce precise data, typically with an accuracy better than ± 1% for major elements (Reed 2005).

Using the electron microprobe as an analytical tool has many advantages, rapid chemical analysis and its imaging capabilities. The electron microprobe can obtain and display high resolution and magnified images of a sample's surface using secondary (SEI) and backscattered electron (BSE) imaging modes. Secondary electron images show the topography of a sample's surface. This imaging tool can be used for identifying the fabric and porosity of grains, microfossils, and grain morphology (Reed 2005). Imaging with backscattered electrons shows compositional information by displaying areas with higher atomic numbers brighter than areas with lower atomic numbers (Reed 2005). Backscattered electron images are very useful for identifying melt inclusions and potential secondary daughter phases within a mineral grain and will be relied on heavily for this study. Another advantage of the electron microprobe is that it is non-destructive. The X-rays generated for analysis do not damage or cause volume loss in a sample (Reed 2005). This allows for multiple analyses to be done on the same spots in a sample while conducting a study. It is possible to collect very localized data because electron microprobes analyze very small spots (microns in size) within a sample (Reed 2005). Also, it allows analysis to be done on sample features that are too small for other analytical techniques like melt inclusions. Again, this will be very beneficial for melt inclusion analysis since melt inclusions are typically 1 – 100 microns wide.

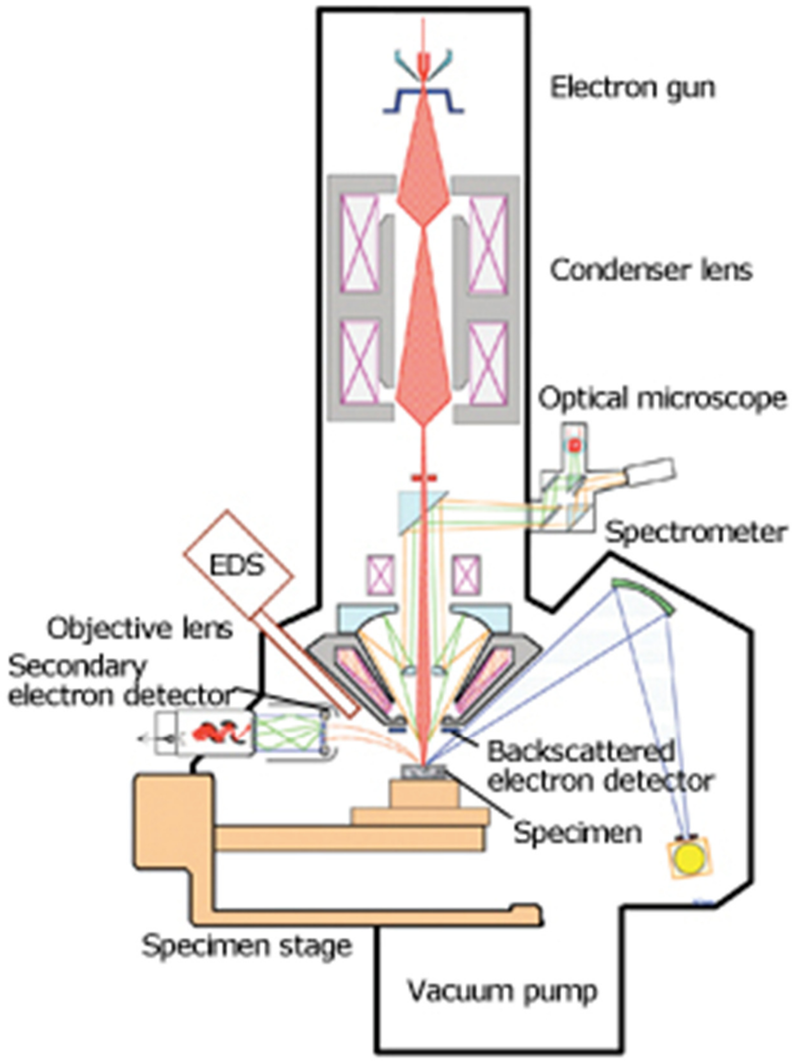

Fig. 10. Schematic drawing of the set up of an electron microprobe (JEOL 2018).

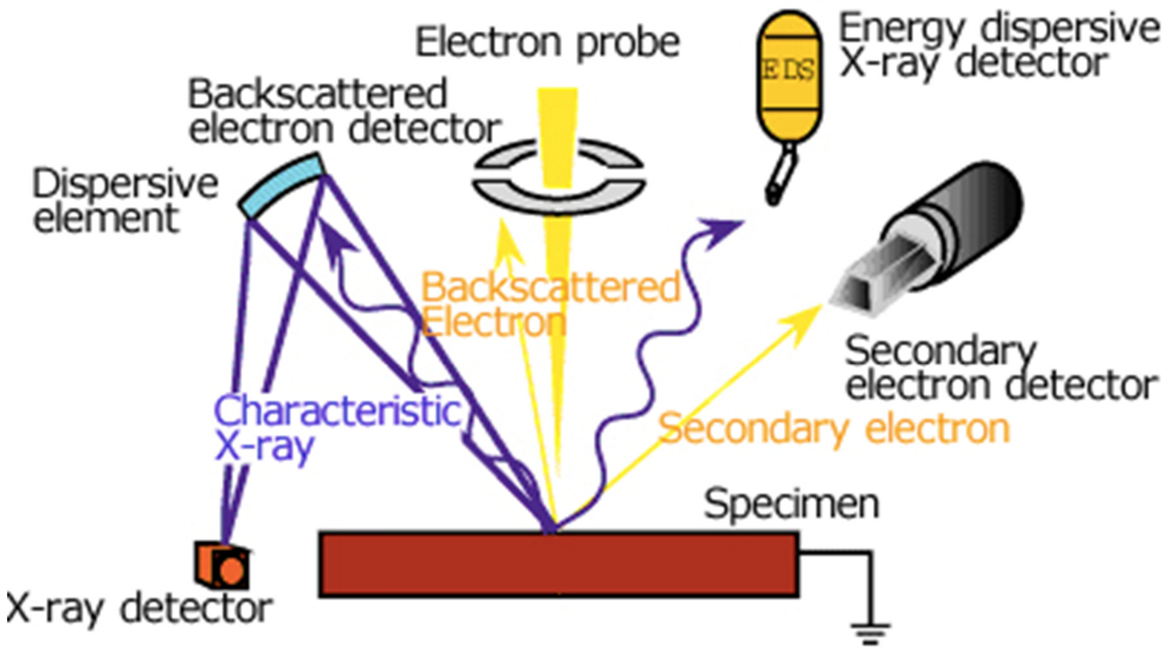

Fig. 11. Schematic drawing of signals generated by an electron microprobe (JEOL 2018).

PREVIOUS RESEARCH

One of the first studies that analyzed melt inclusions from the Bandelier Tuff was performed by Sommer (1977). For his study, he examined melt inclusions in quartz phenocrysts from Plinian fall and ignimbrite units of the Upper Bandelier Tuff. Through electron microprobe and mass spectrometry, Sommer (1977) analyzed the H_2O, CO_2 and CO content of the melt inclusions. The microprobe results showed volatile content ranging from 2.4 – 7 wt% with average of 5.4 wt%. The mass spectrometry gave the value of the volatiles separately and found to be H_2O = 91.9%, CO_2 = 2.7% and CO = 4.8% in total volatiles.

Dunbar and Hervig (1992) conducted the main study on melt inclusions from the Bandelier Tuff (mostly LBT). They analyzed trace elements and H_2O, Cl and F content of melt inclusions in quartz, sanidine, and pyroxene from the Otowi Member to determine magma processes and eruptive style. H_2O content was 3 -5 wt% and F content was 0.12 – 0.20 wt%. Based on the H_2O and F content of the melt inclusions, Dunbar and Hervig (1992) concluded that the Plinian tephra magma and bulk ignimbrite magma underwent different processes. They found that the melt inclusions from the Plinian tephra had higher levels of H_2O and F, which indicate an enrichment of volatiles in the upper portion of the magma chamber and would have caused a strong volatile gradient. Dunbar and Hervig (1992) theorize that the volatile gradient could have influenced the eruptive style of the magma and initially caused the magma to erupt in discrete layers when the gradient was strong. Lastly, there is evidence from trace elements in some melt inclusions that the magma that produced the ignimbrites of the Otowi Member was influenced by a second stage of rhyolite magma injection (Dunbar and Hervig 1992).

Sr isotope studies widely accepted and very accurate for determining origin and formation of igneous rocks, so quite a few studies of $^{87}Sr/^{86}Sr$ ratios have been conducted on the Bandelier Tuff. Wolff et al. (1999) analyzed Rb/Sr and Sr ratios of sanidine, glass, and melt inclusions in quartz from the Otowi Member. Results showed high Rb/Sr ratios (14 to 570) from the sanidine and glass and lower Rb/Sr ratios for the quartz melt inclusions. The quartz melt inclusions were more radiogenic ($^{87}Sr/^{86}Sr_i = 0.7105 - 0.7113$) than the sanidine and glass ($^{87}Sr/^{86}Sr_i = 0.7052 – 0.7056$ and $^{87}Sr/^{86}Sr_i = 0.7052 – 0.7079$) (Wolff et al. 1999). Based on the results, it was proposed that the melt-inclusion-bearing quartz were contaminated more by the surrounding country rock than the sanidine and glass and does not necessarily represent pre-eruptive compositions (Wolff et al. 1999). Wolff et al. (1999) hypothesized that the melt-inclusion-bearing quartz were contaminated more due to forming closer to the magma-country rock contact than the sanidine and glass.

Wolff and Ramos (2014) built on the previous study to determine a more detailed picture of the magma processes that lead to the formation of the Otowi Member of the Bandelier Tuff. They combined Sr and Pb isotope analysis of sanidine, glasses and melt-inclusion-bearing quartz as well as, trace element content of feldspars. Samples showed large variations in $^{87}Sr/^{86}Sr$ (0.70519 - 0.70947), small variations in $^{206}Pb/^{204}Pb$ (17.795 - 17.835) and high $^{87}Rb/^{86}Sr$ due to Sr depletion (Wolff and Ramos 2014). The melt-inclusion-bearing quartz had $^{87}Sr/^{86}Sr$ ratios ranging from 0.7060 to 0.7094. Again the melt inclusions tended to be more radiogenic than the sanidine and the glomerocryst glasses. Wolff and Ramos (2014) stated one possible cause for the more radiogenic melt inclusions is that they grew during a late episode of contamination where quartz growth was greater than sanidine. They also noted that they were unable to reproduce the $^{87}Sr/^{86}Sr$ ratios of melt-inclusion-bearing quartz from Wolff et al. (1999) and suspect that those results were affected by a high blank. The Pb isotope variations indicate that the magma behaved as an open system with country rock and recharge events (Wolff and Ramos 2014). Wolff and Ramos (2014) also suggested that the data indicated three recharge events of high-silica rhyolite and that the last recharge event could have played a part in triggering the eruption of the Otowi Member magma. However, it needs to be noted that these authors only focused on one member of the Bandelier Tuff and did not measure Sr isotopes for the UBT. None of the previous studies have combined analysis of volatile compositions and Sr isotope compositions from the *same* samples.

MATERIALS AND METHODS

Sample Preparation

A total of 12 bags of samples from the Bandelier Tuff were collected during field work in August 2016. Five bags are from the Plinian fall unit of an Otowi Member outcrop (Fig. 12a), four bags are from a Tshirege Member outcrop that is the base ignimbrite unit (Fig. 12b), and three bags are from one of the top ignimbrite units of a separate Tshirege Member outcrop (Fig. 12c). One rock from each bag was selected for analysis. Locations of outcrops where samples were collected can be seen in Figure 3.

To perform TIMS and microprobe analysis, quartz grains had to be extracted from the samples, which took place at Auburn University. First, the rocks were gently crushed with a mortar and pestle. Then the crushed rocks were sieved to ≥1mm and 500µm – 1mm. Next, quartz was picked using a fine-point needle. Only intact quartz grains with euhedral bipyramidal shape were picked to try to obtain unaltered melt inclusions. Samples had to be prepared for whole rock analysis as well. Again, the samples were gently crushed with a mortar and pestle. A majority of the quartz needed to be removed from the samples so they were sieved to ≥53µm. Lastly, the sieved samples were crushed to a powder by an agate mortar and pestle.

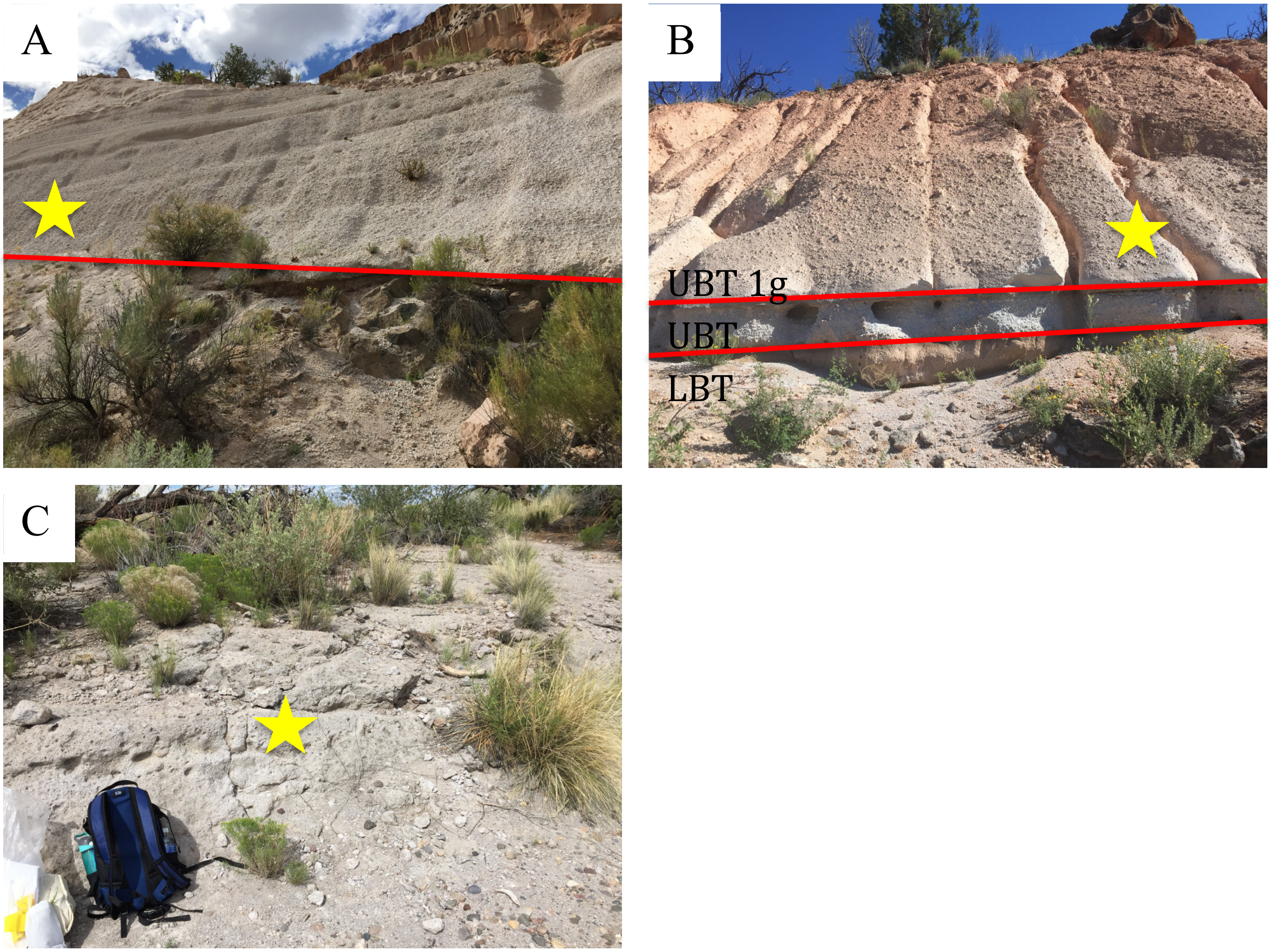

Fig.12. Outcrops of Bandelier Tuff where samples were collected. A) Otowi Member outcrop where BDL 16-7 was collected. B) Tshirege Member outcrop where BDL 16-11 was collected from the uppermost layer. C) Tshirege Member outcrop where BDL 3 was collected. Stars indicate where samples were collected. LBT = Lower Bandelier Tuff unit; UBT = Upper Bandelier Tuff plinian fall unit; UBT 1g = Upper Bandelier Tuff ash flow unit.

Sr Isotope Analysis

After the quartz grains and powdered whole rock samples were obtained from the initial sample preparation process, they had to go through chemical separation so that Sr isotope analysis could be performed by thermal ionization mass spectrometry. The author conducted this work in the trace metal clean room at Auburn University.

1. Sample Preparation

In order to conduct Sr isotope analysis, samples must be specifically prepared to insure the highest possibility of getting quality results. To begin sample preparation, both quartz grains and whole rock powders had to be weighed. Approximately 100 mg of the powder whole rock and ~ 18 mg – 78 mg of the quartz grains were weighed into 7 ml Teflon screw-top capsules. The samples were dissolved by a 3:1 mixture of ultrapure HF and HNO_3 on a hot plate at ~100 °C for a day. After the samples were completely dissolved, the Teflon capsules were placed on a hot plate at ~100 °C overnight with the tops off for evaporation. The final step was separating Sr from the matrix of the samples through column chemistry. This involved cleaning the chromatography columns filled with Eichrom Sr-resin (Fig. 13), loading sample solutions into the columns and then collecting the Sr that was separated by the micro column chromatography process. Once these steps were finished, Sr was left to dry overnight for mass spectrometry. Detailed steps of the chemical separation procedure can be found in Table 1.

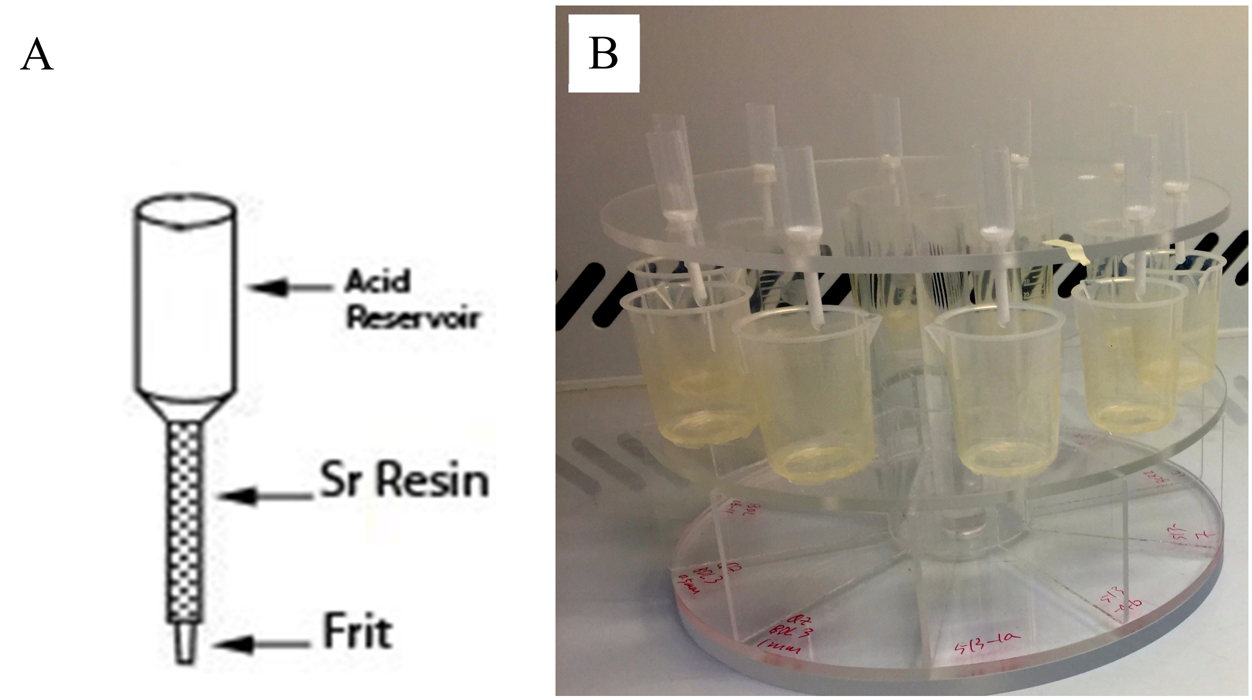

Fig. 13. A) Depiction of column used for chemical separation of Sr (Modified from Li et al 2014). B) Column chemistry set up used for this study.

Table 1.
Chemistry procedure for Sr separation (Modified after Mikova and Denkova 2007).

Procedure	Eluting reagent	Eluting volume (mL)
Cleaning	H_2O	10.0 (5.0 x 2 times)
	0.05 M HNO_3	2.0
	H_2O	5.0
	2 M HNO_3	1.0 (0.05 x 2)
Load sample solutions		
Sr collection	2 M HNO_3	2.5 (0.5 x 5)
	7 N $HNO_3$2 M HNO_3	3.0 (0.5 x 6)2.5 (0.5 x 5)
	3 N $HNO_3$7 N HNO_3	0.53.0 (0.5 x 6)
	0.05 M $HNO_3$3 N HNO_3	2.0 (0.5 x 4)0.5
	0.05 M $HPO_4$0.05 M HNO_3	1 drop2.0 (0.5 x 4)
	0.05 M H_3PO_4	1 drop

2. Thermal Ionization Mass Spectrometer

Strontium isotopic compositions were analyzed by a thermal ionization mass spectrometer (TIMS, Finnigan MAT 262) at the Trace Metal Isotope (TMI) Laboratory at Auburn University for measuring radiogenic and stable isotopes of trace metals (Fig. 14.). The multi-collector MAT 262 is equipped with 8 Faraday cups and a secondary electron multiplier. Purified Sr samples are picked up from Teflon beakers using dilute (0.25 N) HNO_3 and are mixed with 1 microliter TAPH solution (Zou 1999). The mixture is then loaded onto degassed rhenium filaments as ionization filaments. Sr samples on the single thin Re filaments are dried at 0.7 ampere (A). The filament current is then slowly increased to 2.0 A until all H_3PO_4 is evaporated, and finally is flushed very briefly at 3.0 A. Filaments with Sr samples are then mounted to a sample magazine that can hold up to 13 samples. The magazine is loaded to the ion source of MAT-262. Vacuum in the ion source and mass analyzer of the mass spectrometer is kept at below 10^{-7} Torr. Purified Sr samples are thermally ionized by passing a current through the filaments in the ion source. An accelerating voltage of 10 kV is used to accelerate Sr^+ ions from the ion source into the magnetic sector mass analyzer. Dynamic jumping mode is used for Sr isotope analyses. Sr isotopic compositions are normalized to $^{86}Sr/^{88}Sr$ of 0.1194.

<u>Melt Inclusion Analysis</u>

One polished grain mount was made for each sample (BDL 3, BDL 16-7 and BDL 16-11) by the author. Each grain mount had about fifteen ≥1mm quartz grains and about fifteen 500µm-1mm quartz grains. Once the grain mounts were prepared, major elements and sulfur content of the melt inclusions were analyzed by the JEOL JXA 8600 electron microprobe at Auburn University.

Fig. 14. Thermal ionization mass spectrometer (TIMS, Finnigan MAT 262) at the Trace Metal Isotope Laboratory at Auburn University.

Since the electron probe cannot measure H_2O content (H is too light), the indirect sum deficit H_2O method will be used to analyze the H_2O content. This involves measuring all major elements and S. For example, if the total content of all elements is 97.5%, then the deficit 2.5% is considered to be H_2O.

1. Sample Preparation

For microprobe analysis of melt inclusions to be successful, sample preparation has to be very precise. First quartz grains were placed on a piece of double-sided sticky tape with a fine-point needle (Fig. 15a). A one-inch Teflon mold was placed around the grains and a 4:1 mixture of epoxy and hardener was poured into the mold (Fig. 15b). Once the epoxy dried overnight, the Teflon molds were pulled apart from the double-sided sticky tape and the epoxy mounts were pushed out of the Teflon molds. The mounts were then placed in an oven at 60 °C for a few hours so that the epoxy could completely harden. Next, each grain mount was polished so that grain surfaces and melt inclusions were exposed. This was done by using 600, 1000, and 6 μm silicon carbide grit in five-minute intervals until melt inclusions were exposed on grain surfaces (Fig. 16). For thorough cleaning, an ultrasonic cleaner was used to remove all polishing byproducts from the grain mounts. Each grain mount was rinsed with soapy water at two-minute intervals until all grit was removed and then once in alcohol for 30 seconds. After cleaning, the grain mounts were placed in an oven at 60 °C for four hours to dry. Lastly, grain mounts were placed in the SPI – Module Carbon Coater to be coated with carbon to create an electrically conductive surface for microprobe analysis.

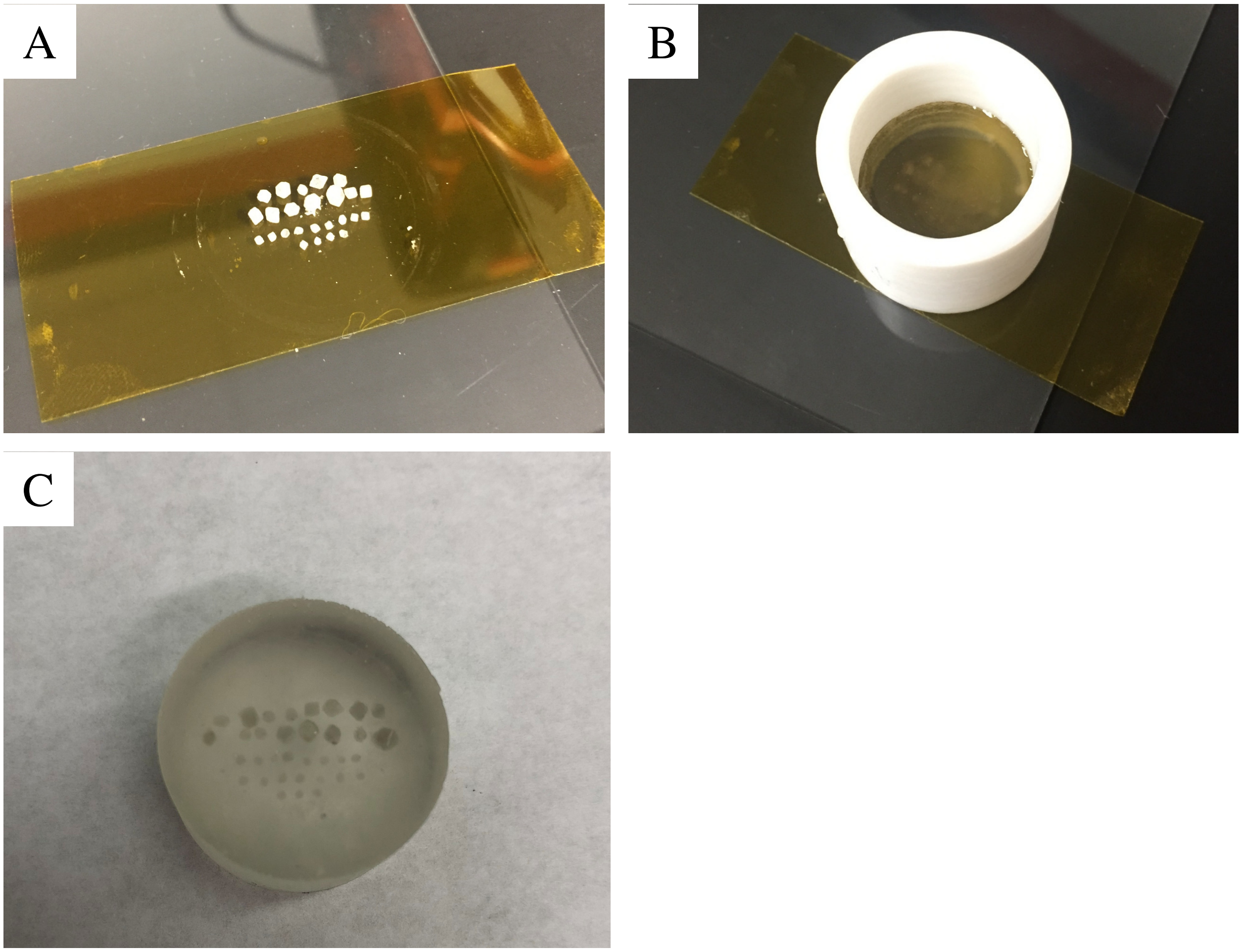

Fig. 15. A) Close up of quartz grains placed on double sided- sticky tape. B) Teflon mold with quartz grains in epoxy. C) Final polished grain mount.

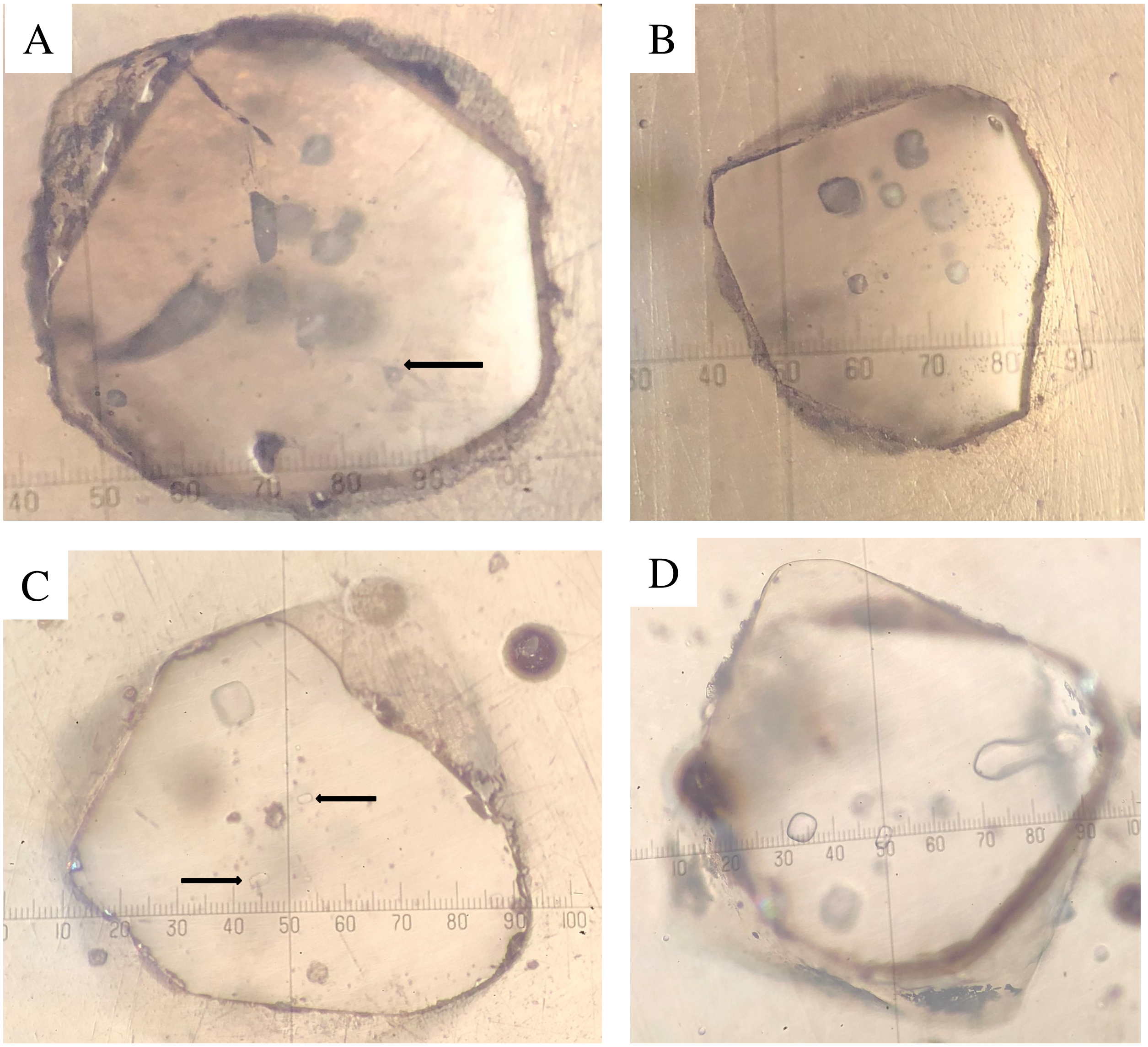

Fig. 16. A) and B) Devitrified melt inclusions in quartz grains from sample BDL 3. Black arrow indicating bubble in melt inclusion. C) and D) Glassy melt inclusions in quartz grains from sample BDL 16 - 7. Black arrows pointing to smaller melt inclusions.

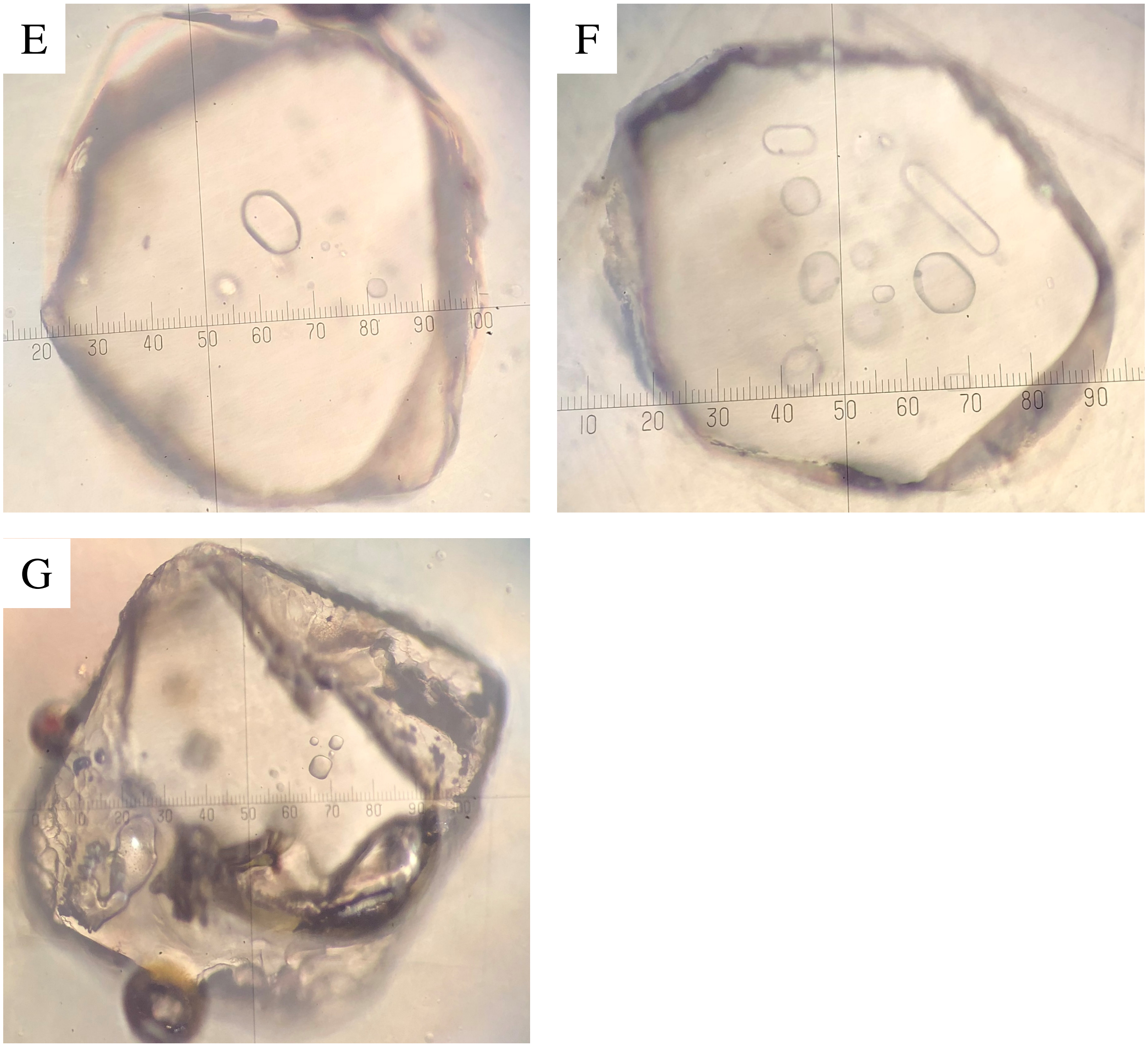

Fig. 16 continued. E) and F) Glassy melt inclusions in quartz grains from sample BDL 16 - 7. G) Small glassy melt inclusions in nicely preserved euhedral bipyramidal quartz grain in sample BDL 16 – 11.

2. Microprobe Analysis

Melt inclusions were analyzed by the JEOL JXA 8600 electron microprobe using an accelerating voltage of 15 kV, a beam current of 20 nA, a beam size of 5 μm and a counting time of 20 sec. Standardization of elements was done through known mineral and glass samples (Albite for Na, VG 568 glass for Si and Al, Olivine for Mg, microcline for K, anorthite for Ca, ilmenite for Ti, garnet for Fe and Mn, pyrite for S and apatite for P). In order to check that the microprobe was measuring major elements and volatiles accurately, the glass standard (VG 568) was analyzed about 6 times every day before analyses of melt inclusions began. Table 2 shows the set for glass analyses. Backscattered electron images (BSE) were used to find melt inclusions in the quartz. Melt inclusions appeared as slightly brighter features than quartz (Fig.17). Once melt inclusions were identified, 1 to 6 points of analysis were conducted for each melt inclusion. Analyses of major element, P and S concentrations were calculated using dQuant software and ZAF matrix corrections.

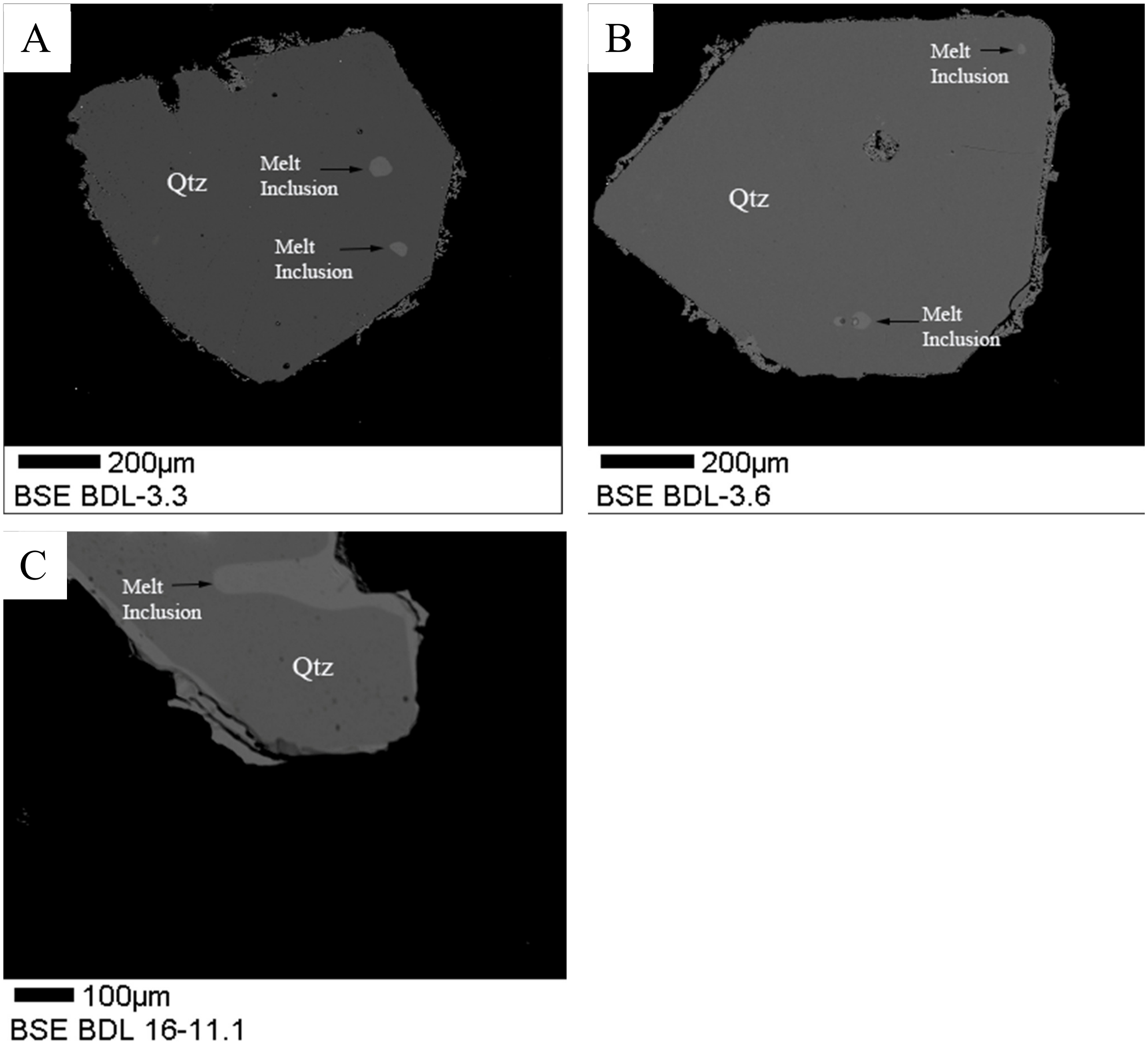

Fig. 17. Backscattered electron images of quartz with melt inclusions. Notice the little BSE contrast between quartz and silica-rich melt inclusions C) Example of "hourglass" melt inclusion.

Table 2. Standard setup for glass analyses.

	Crystal	Spectrometer	Standard
Si	TAP	2	VG 568 Glass
Al	TAP	2	VG 568 Glass
Fe	LIF	4	P130 Garnet
Mn	LIF	4	P130 Garnet
Mg	TAP	1	Springwater Olivine
Ca	PET	3	Anorthite
Na	TAP	1	Amelia Albite
K	PET	3	Mircrocline
S	PET	3	Pyrite
P	PET	3	Wilberfore Apatite

RESULTS

Sr Isotopic Data

$^{87}Sr/^{86}Sr$ ratios of whole rock and melt inclusions in quartz samples for BDL 3, BDL 16 - 7 and BDL 16 -11 can be seen in Table 3. In the table, samples are listed in order of deposition so that it is easier to interpret changes in $^{87}Sr/^{86}Sr$ ratios in chronological order of the two caldera forming events. For each sample two different grain sizes of melt-inclusion-bearing quartz were analyzed to see if $^{87}Sr/^{86}Sr$ ratios varied not only between the whole rock and melt inclusions but between the grain sizes as well. The $^{87}Sr/^{86}Sr$ ratios of whole rock and differing grain sizes of melt-inclusion-bearing quartz are very similar within each sample. This indicates that the melt inclusions represent bulk magma compositions. The data also indicates that the melt inclusions in different quartz grain sizes within each sample do not represent different magma compositions.

Electron Microprobe Data

Major element and volatile contents of melt inclusions from each sample are listed in Tables 4, 5, and 6. The SiO_2 and total alkali ($Na_2O + K_2O$) concentrations in weight percentages of each sample have been plotted on individual TAS diagrams (Figs. 18 – 20). A TAS diagram combining the compositions of melt inclusions from each sample has also been made (Fig. 21). Results show that BDL 3 has the lowest silica content out of the three samples, ranging from 71 to 75 wt%, which plots it as a low silica rhyolite. BDL 16 – 7 and BDL 16 – 11 have higher silica

Table 3.
Sr isotope data for samples BDL 3, BDL 16 – 7, and BDL 16 – 11. (Listed in eruptive order).

Sample		$^{87}Sr/^{86}Sr$	Stratigraphic Unit
BDL 3			Top of Upper Bandelier Tuff
	Glass	0.707134+/-0.000009	
	MIBQ (500µm--1mm)	0.706747+/-0.000030	
	MIBQ (≥1mm)	0.707884+/-0.000029	
BDL 16 - 11			Base of Upper Bandelier Tuff
	Glass	0.708786+/-0.000010	
	MIBQ (500µm--1mm)	0.708182+/-0.000018	
	MIBQ (≥1mm)	0.707439+/-0.000016	
BDL 16 -7			Base of Lower Bandelier Tuff
	Glass	0.709761+/-0.000009	
	MIBQ (500µm--1mm)	0.710578+/-0.000019	
	MIBQ (≥1mm)	0.709487+/-0.000012	

Table 4.
Volatile and major element compositions of melt inclusions from sample BDL 16 – 7. n, number of analysis points averaged.

Sample	BDL 16 – 7.2	BDL 16 – 7.3	BDL 16 – 7.4a	BDL 16 – 7.4b	BDL 16 – 7.5b	BDL 16 – 7.6a	BDL 16 – 7.6b	BDL 16 – 7.9
n	4	1	4	1	6	2	2	6
SiO_2	75.51	73.92	75.21	73.88	74.91	72.77	72.80	75.14
TiO_2	0.03	0.04	0.03	0.07	0.08	0.08	0.05	0.03
Al_2O_3	11.67	11.78	11.90	12.17	12.03	12.0	11.81	11.97
FeO	1.22	1.32	1.22	1.23	1.18	1.22	1.13	1.13
MnO	0.07	0.10	0.08	0.06	0.06	0.07	0.07	0.09
MgO	0.007	0	0.007	0.02	0.01	0	0.003	0.007
CaO	0.21	0.20	0.23	0.26	0.24	0.26	0.26	0.23
Na_2O	1.35	1.63	1.50	1.23	1.50	1.65	1.58	1.43
K_2O	3.18	3.64	3.39	3.60	3.39	3.39	3.28	3.38
P_2O_5 (ppm)	26.8	235	12.5	101	53.7	51	0	21
S (ppm)	40	119	58	0	43	0	17.5	43.8
Total	93.29	92.70	93.62	92.56	93.45	91.48	91.02	93.34
H_2O	6.70	7.30	6.37	7.44	6.54	8.51	8.59	6.65

Table 4 continued.
Volatile and major element compositions of melt inclusions from sample BDL 16 – 7. n, number of analysis points averaged.

Sample	BDL 16 – 7.10	BDL 16 – 7.13	BDL 16 – 7.14a	BDL 16 – 7.14b	BDL 16 – 7.15	BDL 16 – 7.16a	BDL 16 – 7.16b
n	6	4	1	1	4	4	4
SiO_2	75.72	74.76	75.40	76.16	75.05	75.17	75.01
TiO_2	0.05	0.02	0.06	0.04	0.04	0.03	0.04
Al_2O_3	11.76	11.97	12.09	12.15	11.86	12.02	11.91
FeO	1.17	1.21	1.19	1.14	1.20	1.15	1.19
MnO	0.04	0.06	0.06	0.09	0.08	0.06	0.09
MgO	0.011	0.008	0.022	0	0	0.004	0.010
CaO	0.24	0.22	0.25	0.22	0.24	0.23	0.22
Na_2O	1.30	1.48	1.43	1.64	1.41	1.43	1.41
K_2O	3.17	3.33	3.27	3.30	3.21	3.22	3.17
P_2O_5 (ppm)	37.3	28	0	81	16	80.3	85
S (ppm)	190	75.3	33	133	11.3	97.5	17
Total	93.52	93.12	93.80	94.79	93.12	93.36	93.10
H_2O	6.47	6.87	6.20	5.21	6.87	6.63	6.89

Table 5.
Volatile and major element compositions of melt inclusions from sample BDL 16 – 11. n, number of analysis points averaged.

Sample	**BDL 16 – 11.2a**	**BDL 16 – 11.2b**	**BDL 16 – 11.2c**	**BDL 16 – 11.2d**	**BDL 16 – 11.2e**	**BDL 16 – 11.7**
n	5	1	1	2	1	2
SiO_2	77.50	78.34	77.34	77.90	77.53	77.90
TiO_2	0.06	0.11	0.07	0.04	0.03	0.09
Al_2O_3	12.36	12.18	12.29	12.22	11.68	12.27
FeO	1.42	1.39	1.38	1.40	1.35	1.41
MnO	0.08	0.09	0.07	0.11	0.10	0.09
MgO	0.008	0.01	0.02	0.01	0.03	0.004
CaO	0.26	0.29	0.25	0.24	0.28	0.24
Na_2O	1.52	1.80	1.50	1.69	1.67	1.74
K_2O	3.13	3.70	3.69	3.67	3.71	3.63
P_2O_5 (ppm)	38.6	15	0	15	121	37.5
S (ppm)	33.4	0	0	42	10	256
Total	96.56	97.94	96.64	97.31	96.42	97.43
H_2O	3.43	2.06	3.36	2.68	3.58	2.56

Table 6.
Volatile and major element compositions of melt inclusions from sample BDL 3. n, number of analysis points averaged.

Sample	**BDL 3.3a**	**BDL 3.3b**	**BDL 3.4a**	**BDL 3.4c**
n	6	6	4	4
SiO_2	71.93	71.99	75.85	73.65
TiO_2	0.05	0.06	0.04	0.06
Al_2O_3	16.0	15.73	14.49	15.02
FeO	1.91	1.92	1.78	1.75
MnO	0.11	0.11	0.08	0.09
MgO	0.01	0.02	0	0.01
CaO	0.37	0.35	0.18	0.16
Na_2O	3.45	3.68	2.64	2.73
K_2O	5.85	5.97	4.81	5.97
P_2O_5 (ppm)	24.5	49.7	91.8	16.5
S (ppm)	19	38.33	80.75	0
Total	99.71	99.88	99.91	99.47
H_2O	0.28	0.11	0.08	0.52

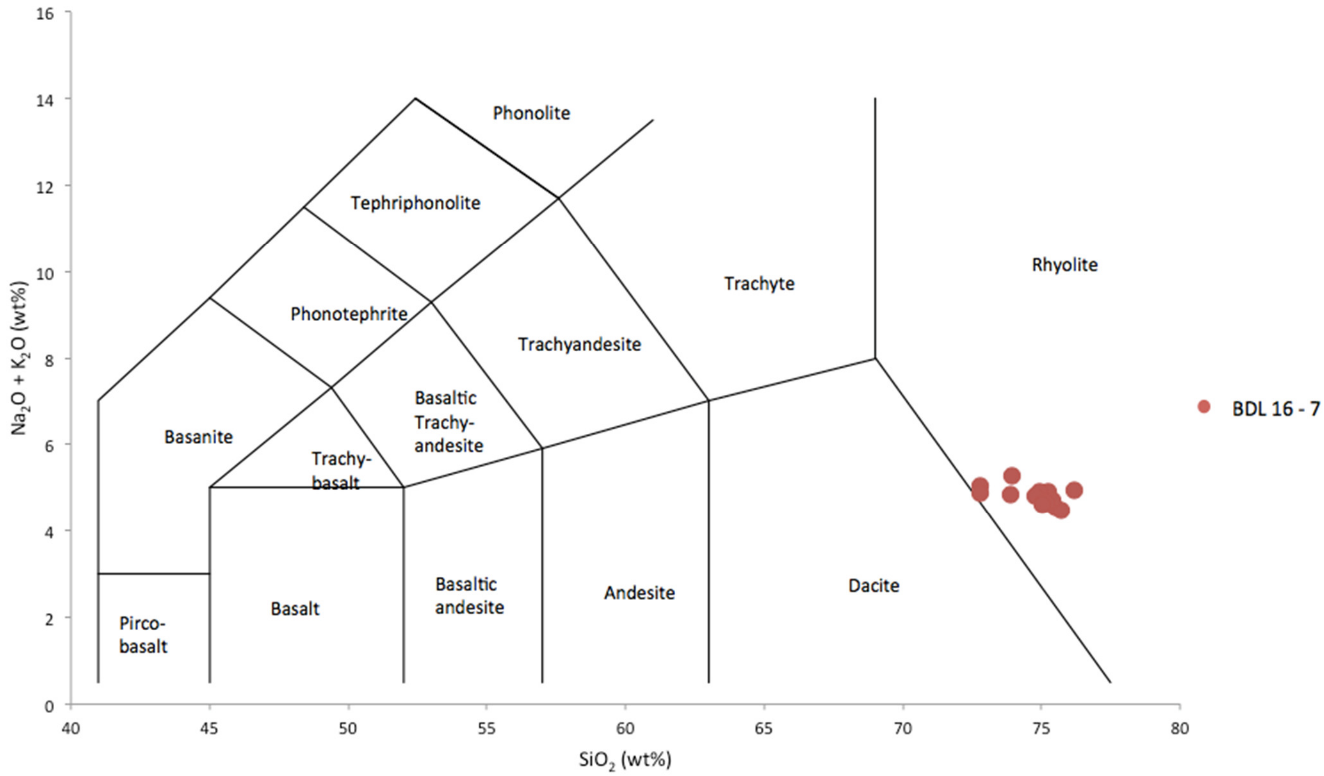

Fig. 18. Total alkali-silica plot of melt inclusions from BDL 16 – 7 indicating a high silica rhyolite composition.

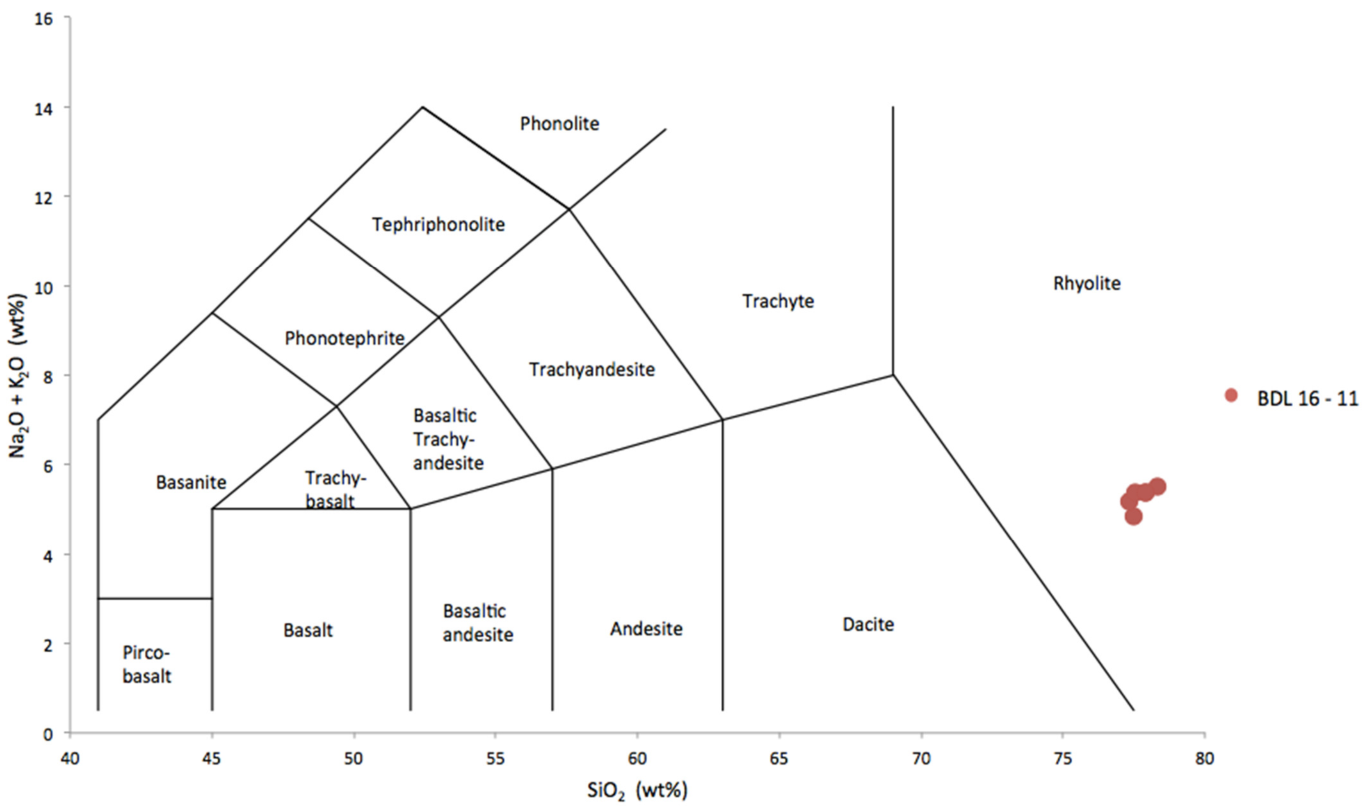

Fig. 19. Total alkali-silica plot of melt inclusions from BDL 16 – 11 indicating a high silica rhyolite composition.

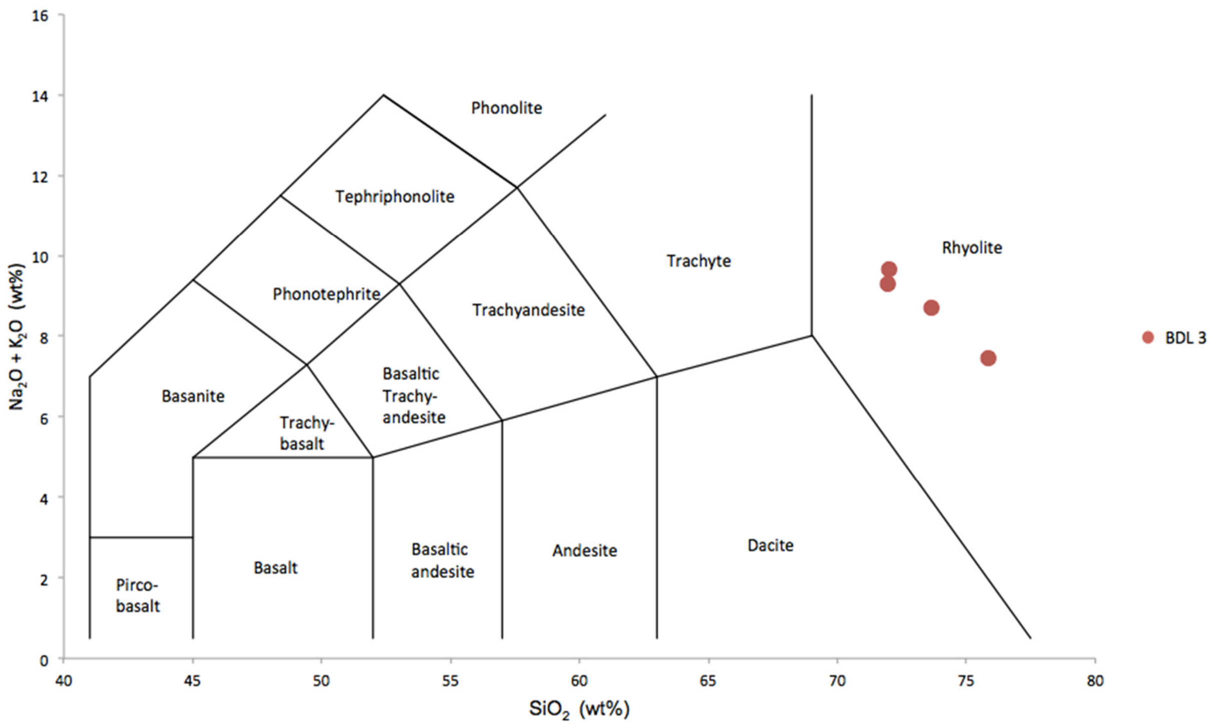

Fig. 20. Total alkali-silica plot of melt inclusions from BDL 3 indicating a low silica rhyolite composition.

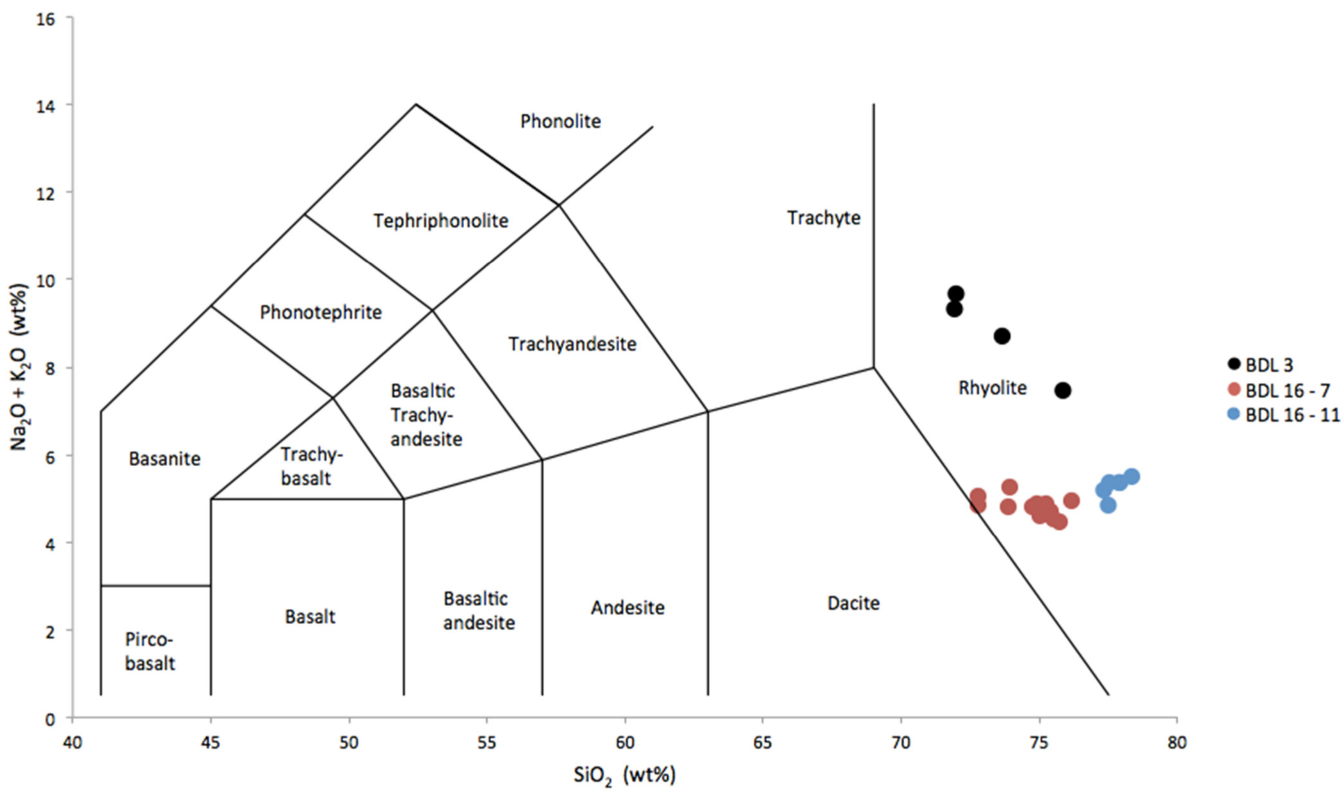

Fig. 21. Total alkali-silica plot of melt inclusions from BDL 16 – 7, BDL 16 – 11, and BDL 3 for comparison.

contents (72 – 76 wt% and 77 – 78 wt%) that give both of them an averaged high silica rhyolite composition.

There is a wide range of variation volatile content varying between the three samples. H_2O content ranges from as high as 8.9 wt% to as low as 0.08 wt%. Sulfur content in all three samples is very low (≤ 256 ppm). Distribution of melt inclusion H_2O content in weight percentage has been plotted against melt inclusion S content in weight percentage for each sample (Figs. 22, 23, and 24). In samples BDL 3 and BDL 16 – 7 there is a slight negative trend, where S content increases, H_2O content decreases. However, in sample BDL 16 – 11 there is no apparent trend between H_2O and S contents. This could be due to the lack of range of S content in this sample's melt inclusions. Figure 25 combines H_2O and S data of all the melt inclusions so that the contents can be compared to one another. BDL 16 – 7 has the highest H_2O content (6.20 – 8.97 wt%) where as BDL 3 has almost no H_2O content (0.08 – 0.52 wt.%). To see if volatile content varies with silica content, H_2O vs SiO_2 plots were made for each sample (Figs. 26, 27 and 28). For BDL 16 -7 and BDL 16 -11 H_2O decreases as SiO_2 increases. There is no trend for sample BDL 3. When plots were made for S vs SiO_2 there was no apparent trend for any sample so plots were not included in the results.

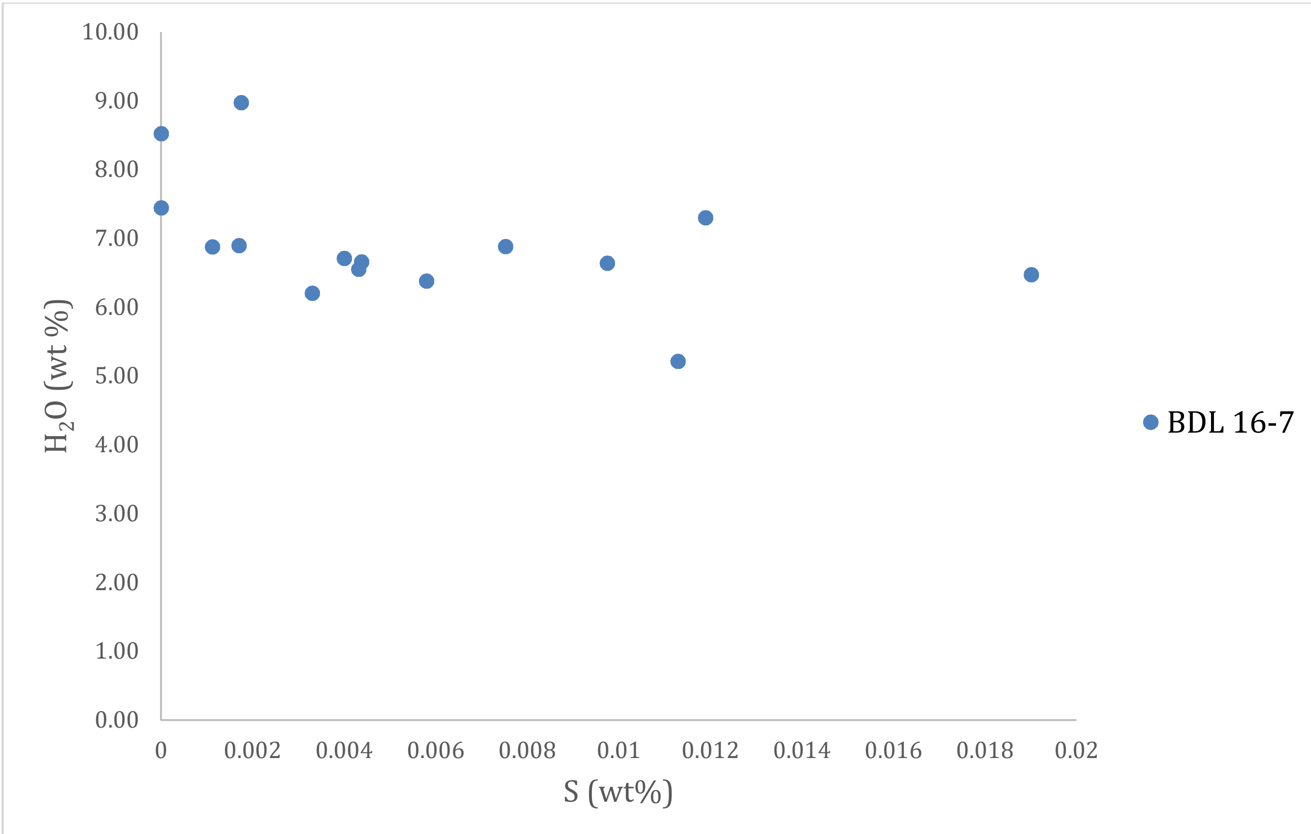

Fig. 22. H_2O versus S of melt inclusions from BDL 16 – 7 showing a negative trend.

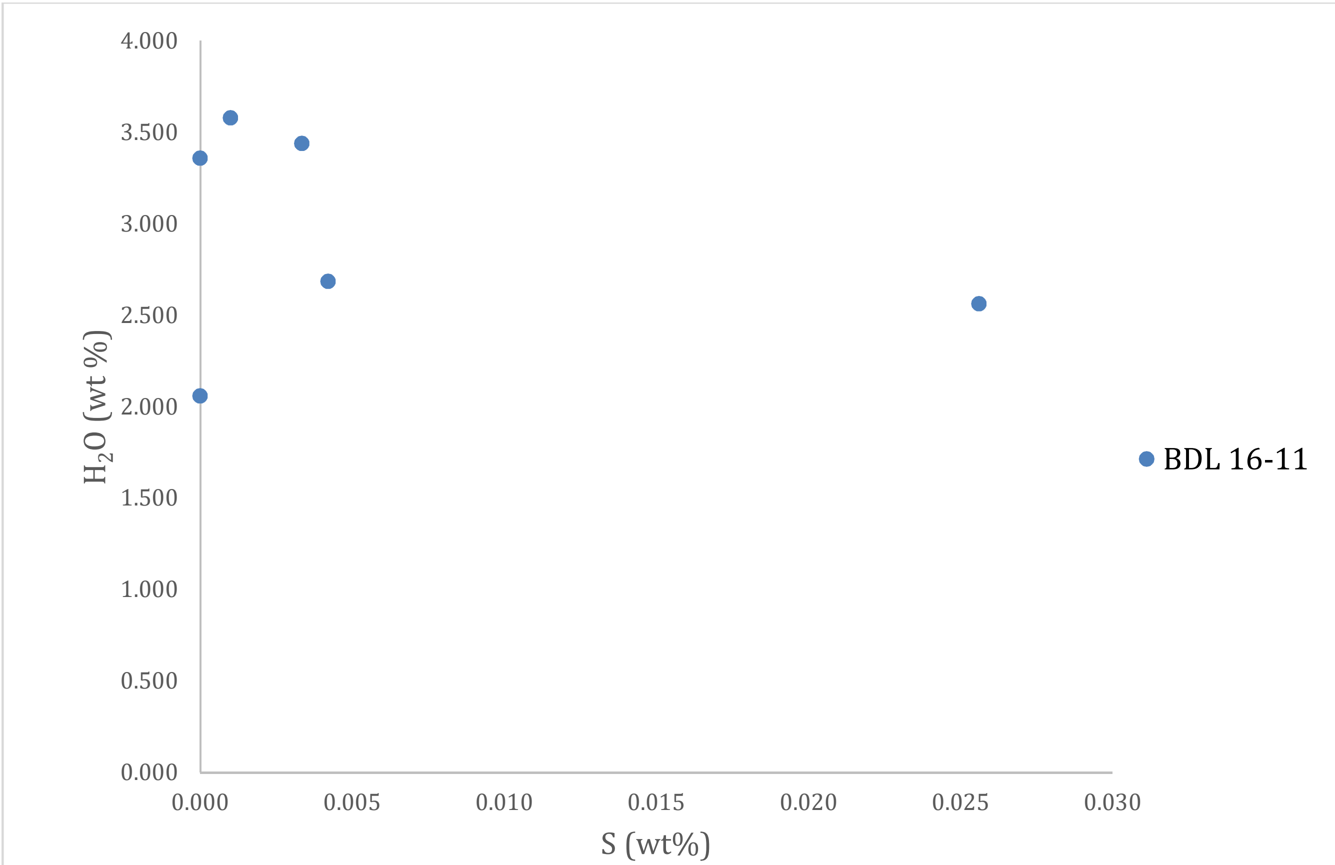

Fig. 23. H_2O versus S of melt inclusions from BDL 16 – 11 showing no apparent trend.

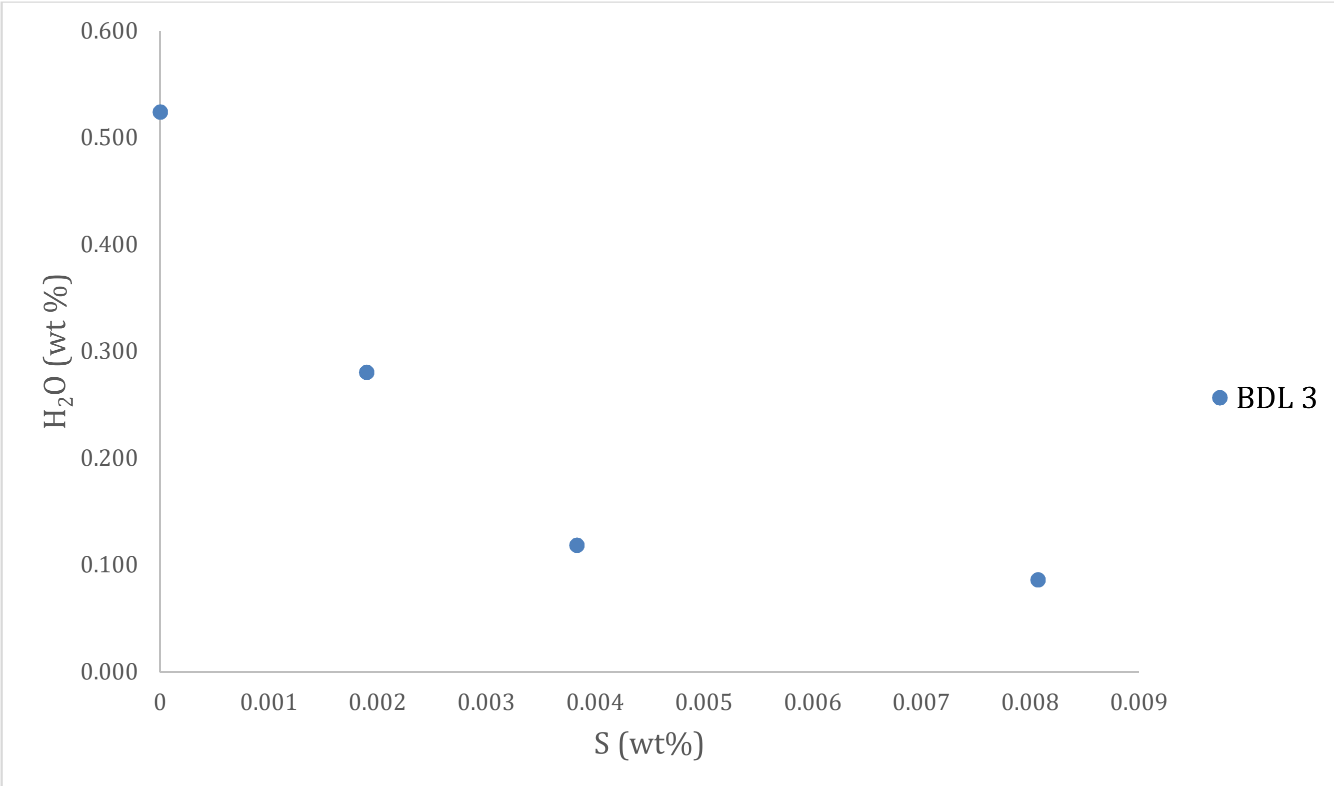

Fig. 24. H_2O versus S of melt inclusions from BDL 3 showing a negative trend.

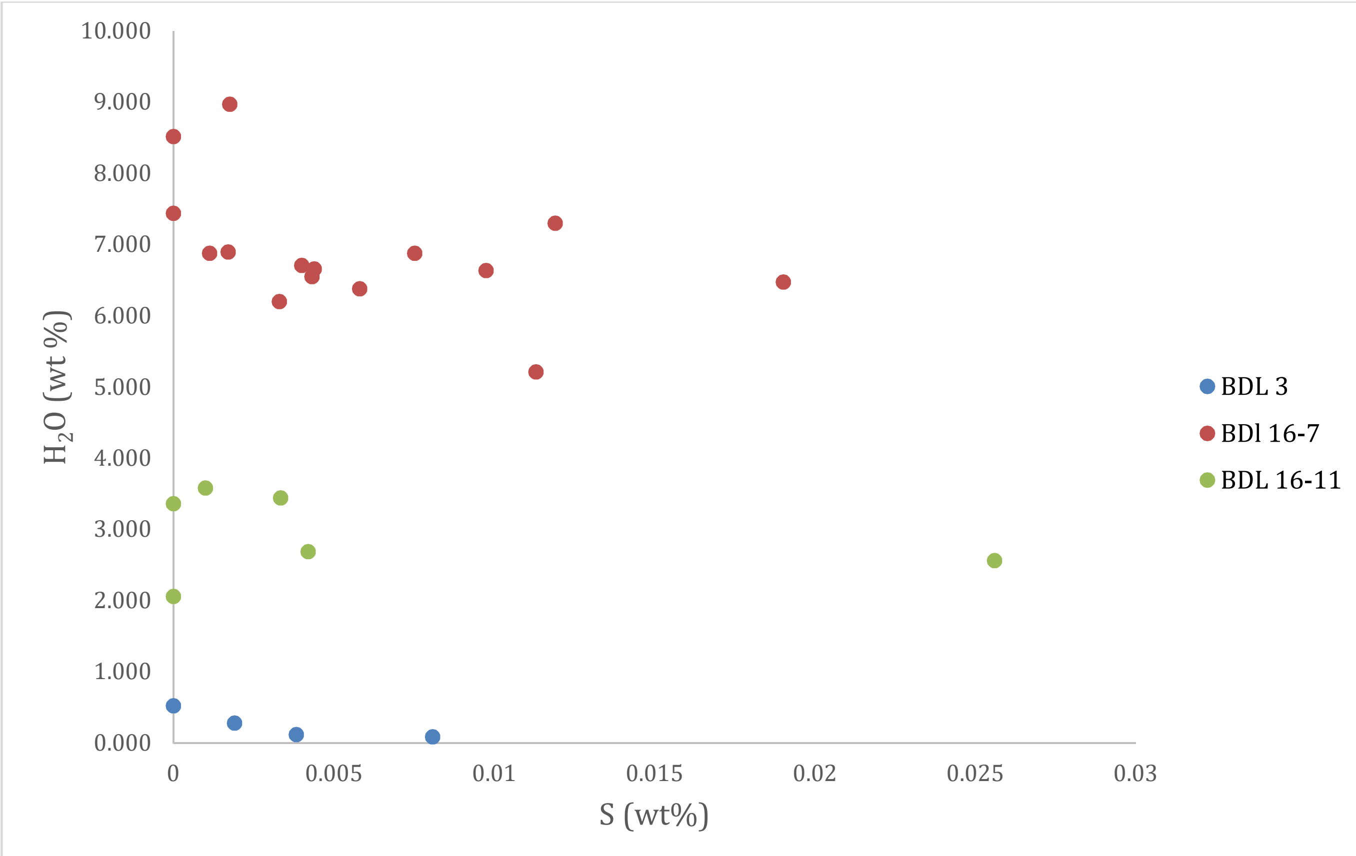

Fig. 25. H_2O versus SiO_2 of melt inclusions from BDL 16 – 7, BDL 16 – 11, and BDL 3 for comparison.

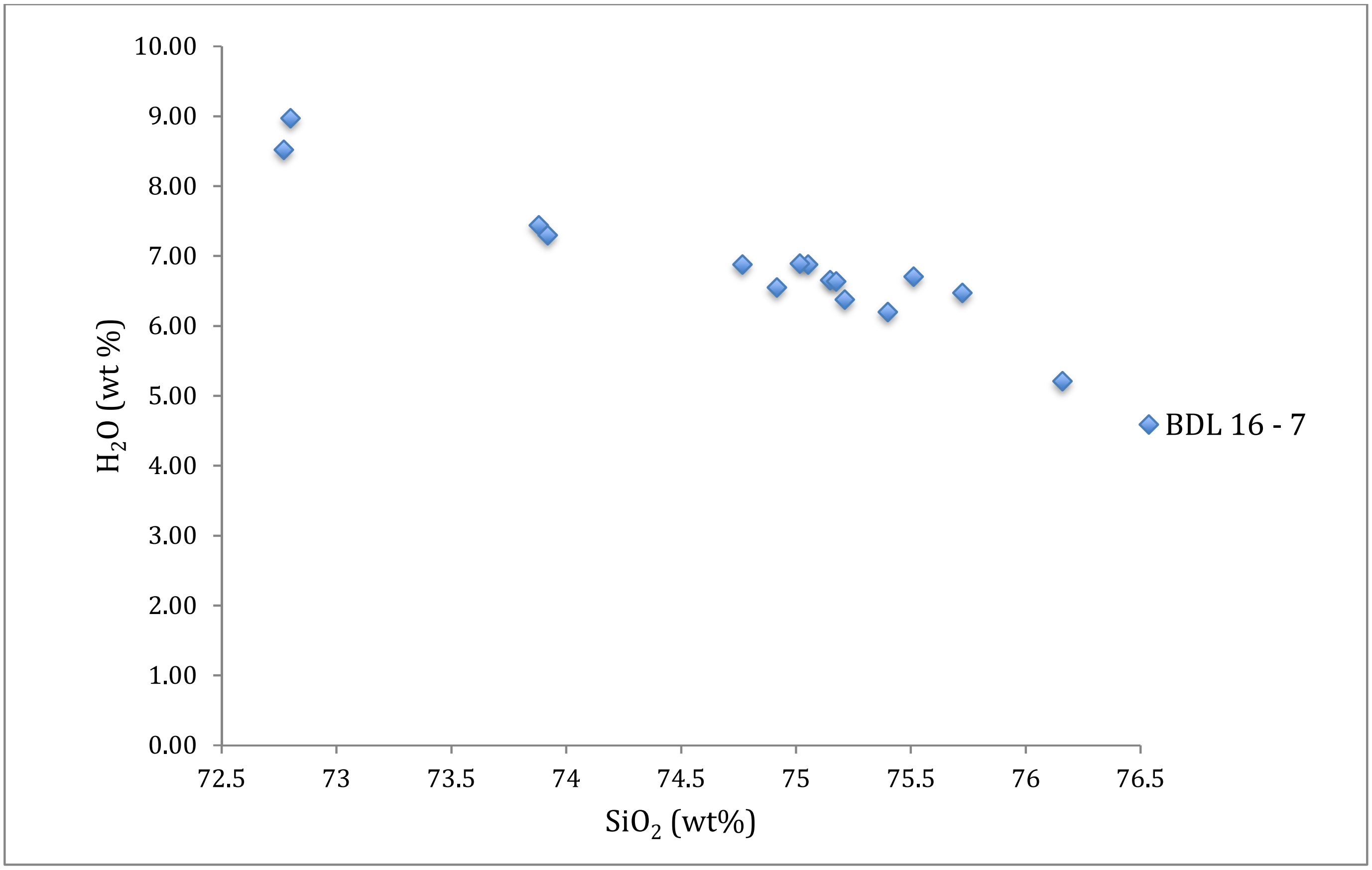

Fig. 26. H_2O versus SiO_2 for melt inclusions from BDL 16 – 7 showing a negative trend.

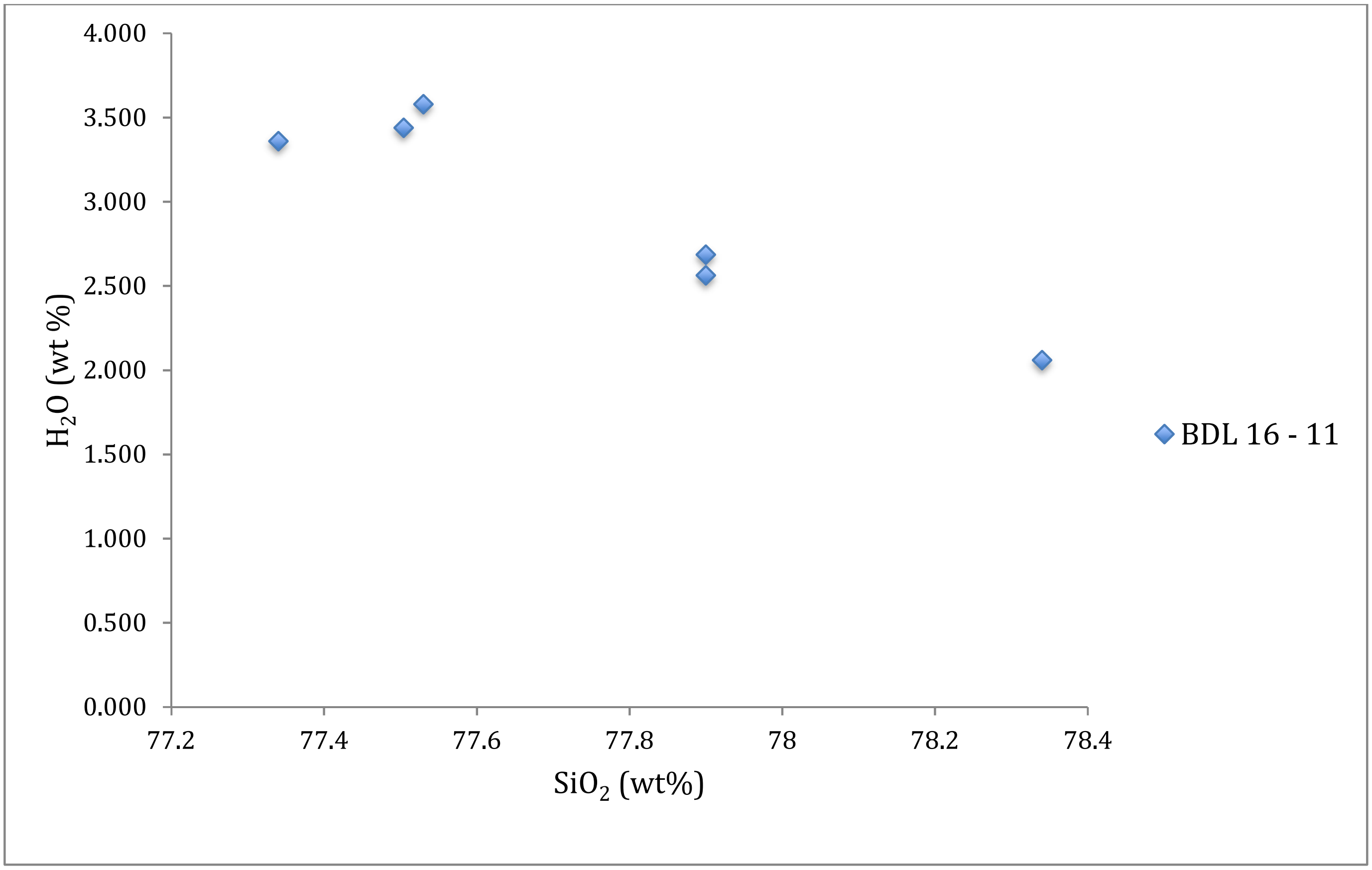

Fig. 27. H_2O versus SiO_2 for melt inclusions from BDL 16 – 11 showing a slight negative trend.

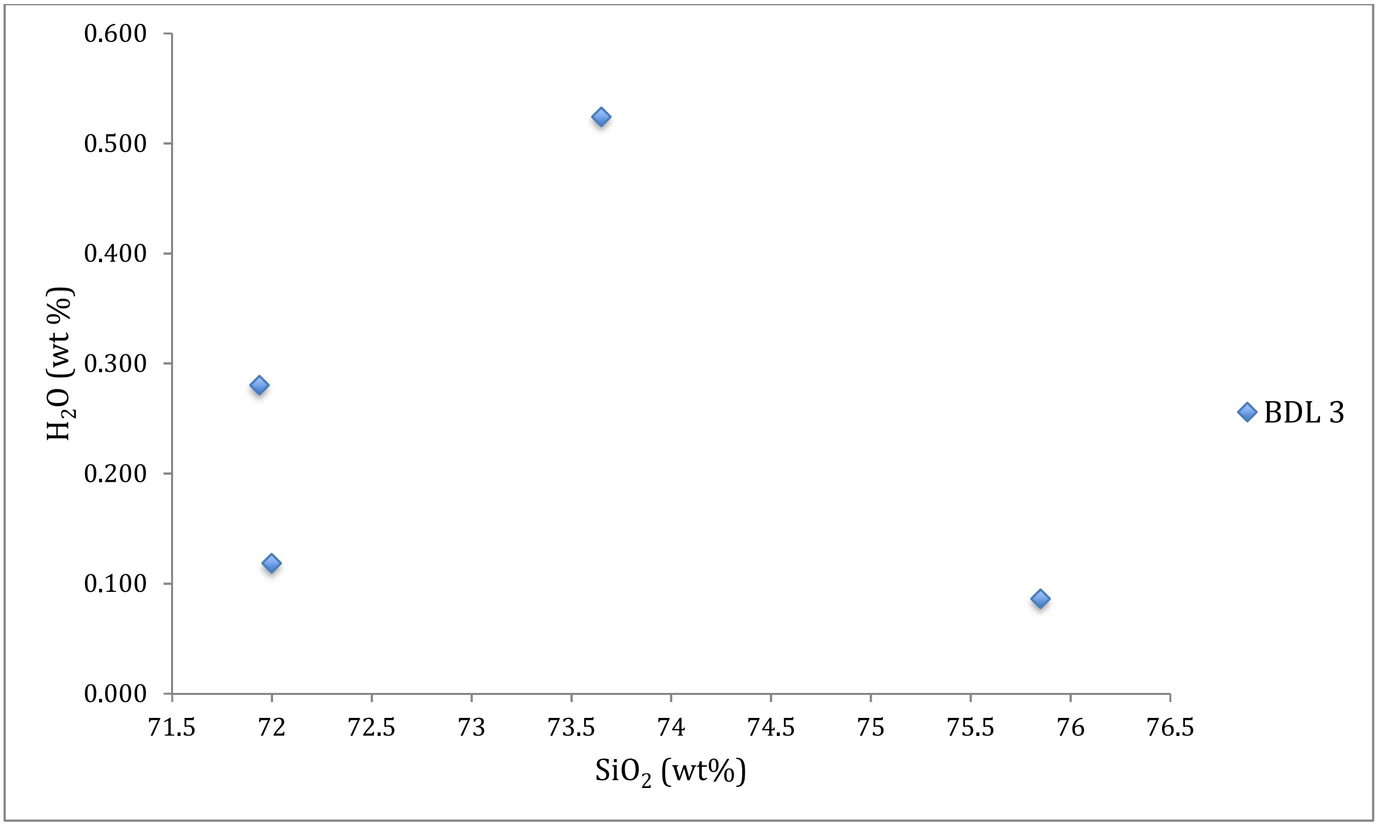

Fig. 28. H_2O versus SiO_2 for melt inclusions from BDL 3 showing no apparent trend.

DISCUSSION

Magmatic Recharge Event

In order to determine if melt inclusions from the Bandelier Tuff represent bulk magma composition, $^{87}Sr/^{86}Sr$ ratios of whole rock were compared to $^{87}Sr/^{86}Sr$ ratios of melt inclusions. The $^{87}Sr/^{86}Sr$ ratios of whole rock and melt inclusions for each sample differ by no more than 0.001, which is a strong indicator that the melt inclusions were in equilibrium with the magma and represent bulk magma composition of respective samples. The small differences in $^{87}Sr/^{86}Sr$ ratios within each sample can be attributed to slight magma heterogeneity within the Bandelier Tuff magma chamber.

However, the differing $^{87}Sr/^{86}Sr$ ratios between each sample are enough to indicate slightly different bulk magma compositions, especially between the Lower Bandelier Tuff and the Upper Bandelier Tuff. BDL 16 -7 (Lower Bandelier Tuff) has the highest $^{87}Sr/^{86}Sr$ ratio (0.710), which makes it the most evolved sample. With $^{87}Sr/^{86}Sr$ ratios of 0.708 and 0.707, BDL 16 – 11 and BDL 3 (Upper Bandelier Tuff) are products of a less evolved magma than BDL 16 – 7. These drops in $^{87}Sr/^{86}Sr$ ratios means that material with a different composition was mixed in with the original magma that produced the Lower Bandelier Tuff. A mantle-derived magma recharge event in the Bandelier Tuff magma chamber after the Lower Bandelier Tuff was erupted is most likely the cause of the lower $^{87}Sr/^{86}Sr$ ratios of the Upper Bandelier Tuff samples. The $^{87}Sr/^{86}Sr$ ratios of the initial Bandelier Tuff magma would lower because mantle-derived magmas have $^{87}Sr/^{86}Sr$ ratios that typically range from 0.702 to 0.706 (Zindler and Hart, 1986; Zou et al., 2000). A mantle-derived magma recharge event is further supported by the $^{87}Sr/^{86}Sr$

ratios of BDL 3. Out of the three samples, BDL 3 was erupted last and therefore came from magma that was further down in the magma chamber. It is very likely that this magma had more interaction with the injected mantle material than the magma at the top of the chamber. This stratification would account for BDL 3 having the lowest $^{87}Sr/^{86}Sr$ ratios and BDL 16 – 11 having slightly higher $^{87}Sr/^{86}Sr$ ratios.

This recharge event could have been the trigger or been a contributing factor to triggering the volcanic eruption that produced the Upper Bandelier Tuff. Folch and Martí (1998) stated that mantle injection and its effects are widely accepted as a trigger for explosive felsic magma events. Secondary effects of mantle injection such as added heat, pressure and magma mixing could have resulted in the residual Lower Bandelier Tuff magma to ascend and erupt once again. When mantle material is injected into a magma chamber, the heat causes exsolution of volatiles from the residual magma (Folch and Martí 1998). The exsolution of volatiles would lower volatile content of the magma and if melt inclusions were trapped after this process then, they too would have lower volatile content. This effect accounts for the progressively lower volatile contents seen in the Upper Bandelier Tuff samples. Exsolution of volatiles would have also contributed to over-pressurizing the magma chamber, which could have led to the second eruption of the Bandelier Tuff.

Volatile Effects on Past and Future Eruptions

Many types of gasses or volatiles are erupted during any volcanic event. H_2O and CO_2 are the main volatiles that control the explosiveness of a volcanic eruption. Other volatiles like sulfur can have significant effects on climate. If enough S is erupted into the atmosphere, it can reflect sunlight and cause a cooling effect.

The Lower Bandelier Tuff sample has high H_2O content (6.20 – 8.97 wt%) and low S content (≤ 190 ppm). Typically, when H_2O content reaches 4 or 5 wt%, volcanic eruptions become explosive. Therefore, the high H_2O content found in BDL 16 – 7 indicates that the volcanic eruption that produced the Lower Bandelier Tuff was very explosive. As for the S content of this member, it is extremely low especially when compared to the S content of a sulfur rich eruption like Mt. Pinatubo. The 1991 eruption of Mt. Pinatubo was the largest volcanic eruption in the past 95 years (Ward 2009). It erupted 491 to 921 megatons of H_2O and melt inclusions had S contents ranging from 260 to 1710 ppm (de Hoog et al. 2004; Ward 2009). The amount of sulfur erupted into the atmosphere caused temperatures to cool by an average of 0.5 °C over a-three-year period (Ward 2009). Based on this effect of the sulfur from Mt. Pinatubo, it is likely that the sulfur from the Lower Bandelier Tuff eruption did not significantly affect the climate.

For the Upper Bandelier Tuff samples, volatiles are slightly lower than the Lower Bandelier Tuff volatiles. These lower volatile contents are likely the result of heat from the mantle-derived magma recharge event removing volatiles in the magma chamber before the eruption. Volatile contents of BDL 16 – 11 and BDL 3 show different extents of this heating effect. Since BDL 3 was erupted last, it was deeper in the magma chamber and closer to the mantle-derived magma recharge. Therefore, the heat affected it more and this interaction is reflected in the volatile contents. BDL 16 – 11 was farther away from the mantle recharge heat and that is why its volatile contents are not as depleted as BDL 3. H_2O content is still high in BDL 16 -11, which was erupted closer to the beginning of the volcanic eruption of the Upper Bandelier Tuff. This indicates that H_2O content was still high enough to be the cause of the second explosive eruption. Again, sulfur contents in both samples were very low so their effect on the climate was minimal.

It is very likely that a future eruption of the Valles Calera will occur since the surrounding area of the caldera is still hydrothermally active. The behaviors of such future eruptions are never easy to predict. However, if the trend of high H_2O content continues then a future eruption could be cataclysmic locally. Also, if H_2O content remains high then it is likely S content will remain low as indicated by Figures 20 and 21. Low S content from a future eruption would not cause significant drop in global mean temperature and society and agriculture would not be heavily affected.

CONCLUSIONS

(1) $^{87}Sr/^{86}Sr$ ratios of bulk rock and melt inclusions in the same sample of the Lower and Upper Bandelier Tuff are similar enough to indicate that melt inclusions are representative of bulk magma compositions.

(2) $^{87}Sr/^{86}Sr$ ratios vary enough between samples, suggesting that the composition of the Lower Bandelier Tuff magma is slightly different than the composition of the Upper Bandelier Tauff magma. A mantle-derived magma recharge event would cause the lower $^{87}Sr/^{86}Sr$ ratios of the Upper Bandelier Tuff Samples.

(3) This mantle recharge event could have contributed to triggering the eruption of the Upper Bandelier Tuff by adding heat and exsolving volatiles in the residual Lower Bandelier Tuff magma. These recharge effects are inferred from the lower volatile contents in the Upper Bandelier Tuff samples.

(4) Volatile contents of all samples suggest that the two caldera forming eruptions were very explosive due to high H_2O content. Sulfur content was low for both caldera-forming eruptions so the effect on climate cooling was probably moderate. If similar volatile trends continue then future eruptions will have explosive eruptions but moderate effect on lowering the temperature by sulfur emissions.

REFERENCES

Bacon, C.R., Newman, S., Stolper, E., 1992. Water, CO_2, Cl, and F in melt inclusions in phenocrysts from three Holocene explosive eruptions, Crater Lake, Oregon. American Mineralogist 77, 1021 – 1030.

Barrabé, L., Deicha, G., 1956. Experiénces de fusion et de cristallisation magmatique sur des reliquats vitreux des quartz dihexaédriques de la Guadeloupe. Bulletin de la Société française de Minéralogie et de Cristallographie 79, 146 – 155.

Cannatelli, C., Doherty, A.L., Esposito, R., Lima, A., De Vivo, B., 2016. Understanding a volcano through a droplet: A melt inclusion approach. Geochemical Exploration 171, 4 - 19.

Chipera, S.J., Goff, F., Goff, C.J., Fittipaldo, M., 2008. Zeolitization of intracaldera sediments and rhyolitic rocks in the 1.25 Ma lake of Valles caldera, New Mexico, USA. Volcanology and Geothermal Research 178, 317 – 330.

Cook, G. W., Wolff, J. A., Self, S., 2016. Estimating the eruptive volume of a large pyroclastic body; the Otowi Member of the Bandelier Tuff, Valles Caldera, New Mexico. Bull Volcanology 70, 10.

Crowe, B. M., Linn, G. W., Heiken, G., Bevier, M. L., 1978. Stratigraphy of the Bandelier Tuff in the Parajito Plateau. Applications to waste management. Los Alamos Scientific Laboratory of the University of California.

de Hoog, J. C. M., Hattori, K. H., Hoblitt, R. P., 2004. Oxidized sulfur-rich mafic magma at Mount Pinatubo, Philippines. Contributions to Mineralogy and Petrology 146, 750 – 761.

Dickin, A.P., 2005. Radiogenic isotope geology: second edition. Cambridge University Press.

Dunbar, N.W., and Hervig, R.L., 1992. Volatile and trace element composition of melt inclusions from the lower Bandelier Tuff: implications for magma chamber processes and eruptive style. Geophysical Research 97, 15, 151–15, 170.

Eichelberger, J. C., Koch, F. G., 1979. Lithic fragments in the Bandelier Tuff, Jemez Mountains, New Mexico. Volcanology and Geothermal Research 5, 115 - 134.

Faure, G. and Mensing, T.M., 2005. Isotopes: Principles and Applications. Third Edition. 897pp.

Folch, A., and Martí, J., 1998. The generation of overpressure in felsic magma chambers by replenishment. Earth and Planetary Science Letters 163, 301 – 314

Frezzotti, M., 2001. Silicate-melt inclusions in magmatic rocks: applications of petrology. Lithos 55, 273 - 299.

Goff, F., and Janik, C.J., 2002. Gas geochemistry of the Valles Caldera region, New Mexico and comparisons with gases at Yellowstone, Long Valley and other geothermal systems. Volcanology and Geothermal Research 116, 299 – 323.

Goff, F., and Gardner, J.N., 2004. Late Cenozoic geochronology of volcanism and mineralization in the Jemez Mountains and Valles Caldera, north central New Mexico. Geological Society of New Mexico, 295 – 312.

Goff, F., Warren, R.G., Goff, C.J., Dunbar, N., 2014. Eruption of reversed-zoned upper tshirege member, Bandelier Tuff from centralized vents within Valles caldera, New Mexico. Volcanology and Geothermal Research 276, 82 – 104.

Golombek M.P., McGill G.E., Brown L., 1983. Tectonic and geologic evolution of the Española Basin, Rio Grande rift: Structure, rate of extension, and relation to the state of stress in the western United States. Tectonophysics 94, 483 – 507.

Hauri, E.H., Kent, A.J.K., Arndt, N., 2002. Melt inclusions at the millennium: toward a deeper understanding of magmatic processes. Chemical Geology 182, 1 – 3.

Horwitz, E. P., Chiarizia, R., Dietz, M. L., 1992. A novel strontium-selective extraction chromatographic resin. Solvent Extraction and Ion Exchange 10, 313-336.

"JEOL Electron Probe Micro Analyzer Home Page." https://www.jeol.co.jp/en/science/epma.html. Accessed January 24, 2018.

Li, C. –F., Guo, J. –H., Yang, Y. –H., Chu, Z. –Y., Wang, X. –C., 2014. Single-step separation scheme and high-precision isotopic ratios analysis of Sr–Nd–Hf in silicate materials. Analytical Atomic Spectrometry 29, 1467 – 1476.

Lipman, P.W., 1997. Subsidence of ash-flow calderas: relation to caldera size and magma chamber geometry. Bulletin of Volcanology 59, 198 – 218.

Mikova, J. and Denkova, P., 2007. Modified chromatographic separation scheme for Sr and Nd isotope analysis in geological silicate samples. Geosciences 52, 221-226.

Phillips, E. H., Goff F., Kyle P. R., McIntosh W. C., Dunbar N. W., Gardner J. N., 2007. The $^{40}Ar/^{39}Ar$ age constraints on the duration of resurgence at the Valles caldera, New Mexico. Geophysical Research 112.

Potts, P.J., 1987. A handbook of silicate rock analysis. Springer, Dordrecht.

Reed, S.J.B., 2005. Electron microprobe analysis and scanning electron microscopy in geology. Cambridge University Press.

Roedder, E., 1979. Origin and significance of magmatic inclusions. Bulletin de Mineralogie 102, 487 – 510.

Roedder, E., 1984. Fluid Inclusions. Reviews in Mineralogy 12, Mineralogical Society of America, 644p

Rowe, M.C., Wolff, J.A., Gardner, J.N., Ramos, F.C., Teasdale, R., Heikoop, C.E., 2007. Development of a continental volcanic field: Petrogenesis of pre-caldera intermediate and silicic rocks and origin of the Bandelier magmas, Jemez Mountains (New Mexico, USA). Petrology 48, 2063 – 2091.

Self, S., Heiken, G., Sykes, M. L., Wohletz, K., Fisher, R. V., Dethier, D. P., 1996. Field excursions to the Jemez Mountains, New Mexico.

Stefano, C.J., Mukasa, S.B., Andronikov, A, Leeman, W.P., 2011. Water and other volatile systematics of olivine-hosted melt inclusions from the Yellowstone hotspot track. Contributions to Mineralogy and Petrology 161, 615–633.

Stimac, J., Hickmott, D., Abell, R., Larocque, A.C.L., Broxton, D., Gardner, J., Chipera, S., Wolff, J., Gauerke, E., 1996. Redistribution of Pb and other volatile trace metals during eruption, devitrification, and vapour-phase crystallization of the Bandelier Tuff, New Mexico. Volcanology and Geothermal Research 73, 245–266.

Student, J.J., and Bodnar, R. J., 2004. Silicate melt inclusion in porphyry copper deposits: identification homogenization behavior. The Canadian Mineralogist 42, 1583 – 1599.

Sommer, M.A., 1977. Volatiles H_2O, CO_2 and CO in silicate melt inclusions in quartz phenocrysts from the rhyolitic Bandelier air-fall and ash-flow tuff, New Mexico. Geology 85, 423 – 432.

Sorby, H. C., 1858. On the microscopic structure of crystals, indicating the origin of minerals and rocks. Geological Society of London 14, 453 – 500.

Wallace P. J., Anderson, A.T., Davis, A. M., 1999. Gradients in H_2O, CO_2, and exsolved gas in a large-volume silicic magma system: interpreting the record preserved in melt inclusions from the Bishop Tuff. Geophysical Research 104, 20097 – 20122.

Ward, P. L., 2009. Sulfur dioxide initiates global climate change in four ways. Thin Solid Films 517, 3188 – 3202.

Wilcock, J., Goff, F., Minarik, W. G., Stix, J., 2013. Magmatic recharge during the formation and resurgence of the Valles Caldera, New Mexico, USA: Evidence from quartz compositional zoning and geothermometry. Petrology 54, 635 – 664.

Wilson, M., 1989. Igneous Petrogenesis. Chapman and Hall.

Wolff, J. A., Ramos, F. C., Davidson, J. P., 1999. Sr isotope disequilibrium during differentiation of the Bandelier Tuff: constraints on the crystallization of a large rhyolitic magma chamber. Geology 27, 495 – 498.

Wolff, J. A., Balsley, S. D., Gregory, R. T., 2002. Oxygen isotope disequilibrium between quartz and sanidine from the Bandelier Tuff, New Mexico, consistent with a short residence time of phenocrysts in rhyolitic magma. Volcanology and Geothermal Research 116, 119 – 135.

Wolff, J. A., and Ramos, F.C., 2014. Processes in caldera-forming high silica rhyolite magma: Rb-Sr and Pb isotope systematics of the Otowi Member of the Bandelier Tuff, Valles Caldera, New Mexico, USA. Petrology 55, 345 - 375.

Zindler, A. and Hart, S. R., 1986. Chemical Geodynamics. Annual Review of Earth and Planetary Sciences 14, 493-571.

Zou, H.B., 1999. Studies of mantle melting process and compositions using major and trace elements, Nd-Sr-Pb isotopic systematics and U-series disequilibria: Mathematical modeling and experimental analyses. Ph.D. Thesis, Florida State University, 185pp.

Zou, H.B., Zindler, A., Xu, X.S., Qi, Q., 2000. Major and trace element, and Nd-Sr-Pb isotope studies of Cenozoic basalts in SE China: mantle sources, regional variations, and tectonic significance. Chemical Geology 171, 33-47.